International Journal of Coal Geology 310 (2025) 104870

Contents lists available at ScienceDirect

International Journal of Coal Geology

journal homepage: www.elsevier.com/locate/coal

The modes of occurrence, distribution and enrichment of critical raw materials (Ga, Sr, Zr and Ba) within coal discards of the Witbank Coalfield, South Africa

X. Nkwamza *, N. Malumbazo

School of Chemical and Metallurgical Engineering, Richard Ward Building, University of Witwatersrand, 1 Jan Smuts Avenue, Braamfontein, Johannesburg 2000, South Africa

ARTICLE INFO

Keywords:
Witbank Coalfield
Critical raw materials
Coal discards
Distribution and enrichment

ABSTRACT

Coal mineralogy and trace element composition provide vital insights into the geological coal formation processes, depositional environments, and potential resource valorization. However, there is limited knowledge and understanding of the geochemical and mineralogical composition of coal discards from the Witbank Coalfield. Thus, the coal discards remain underexplored, limiting effective management and future utilization strategies. To address this gap, this study investigates the occurrence, distribution and enrichment of CRMs within Permian coal discards of the Witbank Coalfield. An integrated suite of analytical techniques such as TGA, Bomb calorimeter, FTIR, XRD, TIMA, SEM-EDS, XRF and ICP-MS was utilized to determine the dominant mineral assemblages and trace elemental enrichments. Results revealed quartz and kaolinite as the principal minerals, with subordinate carbonate and sulfide phases introduced through diagenetic and hydrothermal processes. The coal discards were enriched in trace elements such as Ga, Sr, Zr and Ba. Ga was associated with kaolinite and organic matter, Sr and Ba predominantly occurred in barite, and Zr was hosted primarily in detrital zircon grains. Their spatial variability reflects depositional and diagenetic controls. Geochemical proxies, such as Sr/Ba and TiO_2/Al_2O_3 ratios, indicate freshwater depositional conditions influenced by volcanic ash input and post-depositional alteration. These findings enhanced the understanding of the geochemical cycling within coal discards, their mineralogical stability, and potential environmental implications. Furthermore, the presence of acid-neutralizing minerals supports the potential use of these coal discards in mitigating acid mine drainage, while the enriched CRMs highlight opportunities for sustainable resource recovery.

1. Introduction

Critical raw materials (CRMs) are a group of elements that are in high demand, difficult to replace, and have a substantial risk associated with their supply and security (Ferro and Banollo, 2019). These materials are essential in driving various economic sectors, ranging from energy production to advanced technologies underpinning the fourth industrial revolution. The global demand for CRMs is rapidly increasing due to their widespread applications (Dai and Finkelman, 2018) and is inevitably driven by world population growth and the improvement in the standard of living (Lin et al., 2018b). These CRMs are extensively used in electronics, emerging innovations, health care, oil refinery, steel, automotive, aerospace, defense, clean and high-tech products (Ferro and Banollo, 2019; Lin et al., 2018a). These are rare materials which include barium (Kolker et al., 2021; Hao et al., 2022), zirconium (Dai et al., 2011, 2015; Li et al., 2016; Lin et al., 2018a; Yuan et al., 2019; Zhao et al., 2019; Kolker et al., 2021), strontium (Li et al., 2016; Liu et al., 2021), lithium (Li et al., 2016; Zhao et al., 2019a; Kolker et al., 2021; Shao et al., 2022; Wang et al., 2022), uranium (Wang et al., 2021), germanium (Jiu et al., 2021; Davison and Van Rythoven, 2023), and rare earth elements (Lin et al., 2018; Zhao et al., 2019; Shao et al., 2022). Geologically, these materials are found in ore deposits; however, their conventional ore deposits have been exploited and utilized extensively. Therefore, it is crucial to seek other alternative sources such as coal and coal-bearing sequences. Coal is strategically important in logistics due to its widespread availability and dual role as both an energy source and a reservoir of valuable metal and rare earth elements. This makes coal a cost-effective and accessible source for critical materials needed in clean

* Corresponding author.
E-mail address: 1533778@students.wits.ac.za (X. Nkwamza).

https://doi.org/10.1016/j.coal.2025.104870
Received 26 May 2025; Received in revised form 28 August 2025; Accepted 28 August 2025
Available online 1 September 2025

energy technologies, reducing reliance on traditional mining and geopolitical risks (Seredin and Finkelman, 2008; Seredin et al., 2013; Dai et al., 2018a).

Coal discards are low-grade materials produced from coal mining and beneficiation as waste, and like coal, they are rich in minerals and organic matter (Falcon and Ham, 1988; Orem and Finkelman, 2005; Misz-Kennan and Fabiańska, 2011; Vo et al., 2022). They have a complex pore structure as well as distinct physicochemical properties (Falcon and Falcon, 1987). Additionally, their inherent adsorptive and reduction behavior is attributed to the presence of trace elements (Dai and Finkelman, 2018). Recent studies have identified coal seams globally enriched in critical raw materials such as Ba (Zhao et al., 2014), Sr (Liu et al., 2021), REY (rare earth elements and yttrium; Hower et al., 2018; Mastalerz et al., 2020; Shao et al., 2022; Rerani et al., 2024), and Li (Shao et al., 2022; Wang et al., 2022), some exceeding economically viable cut-off grades. Aluminium and gallium have been economically extracted from coal since 2018 (Seredin, 2012; *China Science and Technology Daily Report*, 2018), while Ge and U have also been industrially extracted from coal ash (Dai et al., 2012a, 2014a; Dai and Finkelman, 2018). However, there is minimal research conducted on the presence of CRMs from the South African coal discards, especially the Witbank Coalfield.

A complete understanding of the geological distribution and enrichment of the critical raw materials in coal is known to be predominantly controlled by several geological factors such as source materials, marine environment, hydrothermal fluids, groundwater and volcanic ash (Dai et al., 2012a). For instance, hydrothermal fluids derived from magmatic activities have been associated with elevated Li and REE concentrations in Pennsylvanian anthracite coals, whereas marine transgressions influence elements such as Mo, U, Se, and Re (Zhao et al., 2019). Similarly, the enrichment of the Li, Ga, and REEs in the upper coal of Datong Coalfield was due to weak seawater influence (Shao et al., 2022).

The Witbank coal is known to be enriched in trace elements such as Co, Zn, As, Se, Sr, Yb, Zr, Ba, Pb, W and U (Pinetown, 2007; Netshitungulwana et al., 2022). Additionally, Ti, Mn, and Fe have been documented by Maya et al. (2015), while REY + Sc were highlighted by Modiba and Wagner (2024). Although the modes of occurrence, distribution patterns, and enrichment mechanisms of these elements in coal and ash are well understood globally, their behavior in coal discards remains poorly studied, especially in the South African context. In addition, it is important to understand the presence of critical raw materials in coal discards, as they are becoming both an economic burden to the government and a health hazard to surrouding communities. This is because coal discards can undergo weathering, oxidation, and hydrogeochemical processes that alter the speciation, mobility, and enrichment patterns of trace elements. Therefore, understanding the occurrence, distribution, and enrichment of Ga, Sr, Zr and Ba in coal discard dumps is critical for assessing potential environmental risks and exploring opportunities for secondary resource recovery. Furthermore, South Africa does not have the geological reserves and resources to mine Ga, Sr, Zr and Ba. The scientific findings of this paper could potentially boost the country`s commodity markets.

This study aims to address the above-mentioned knowledge gaps by investigating the occurrence, distribution, and enrichment of CRMs in coal discards from the Witbank Coalfield. In doing so, the study will clarify the geological processes influencing CRM concentrations, assess their potential for resource recovery, and provide scientific insights which are vital for the sustainable management and utilization of coal discards. By highlighting the novel occurrence of these elements and offering an in-depth geochemical assessment, this research will contribute to advancing CRM exploration from unconventional secondary sources. This will further advance the potential beneficiation strategy of the CRMs in coal discards.

2. Geological setting

The Witbank Coalfield is located in the northeastern part of Mpumalanga province, South Africa (Fig. 1). The geological framework of this coalfield is dominated by a sequence of undeformed to low-grade metamorphosed volcanic rocks, shales, quartzites, mudrocks, sandstones, dolomites, banded iron formations, conglomerates, and diamectites belonging to the Selon River formation (Eriksson et al., 1993; Eriksson and Altermann, 1998). Overlying this formation are the organic-rich sandstones, shales, coal beds, mudstones, siltstones, and minor conglomerates of the Vryheid Formation (Jones and Wagener, 2017; Soeder and Borglum, 2019).

Structurally, this coalfield is situated in the northern part of the Main Karoo Basin (MKB), an area characterized by extensive valleys and ridges shaped by glacial erosion. These landforms bear the imprints of ice sheets that once traversed the Gondwana region during Palaeozoic glaciations (Hancox and Götz, 2014). Within the coalfield, five major NNE-SSW trending paleovalleys have been delineated: Grootvlei, Vischkuil, Coronation, Bank, and Arnot. The Grootvlei Valley extends southward from north of Nigel towards the South Rand Coalfield. Vischkuil Valley trends from the northeast of Springs to Devon. Coronation Valley runs from north of the Coronation Kromdraai Colliery southwards to Springbok Colliery and the southeast towards Hendrina. Bank valley stretches from northwest of Middelburg south to Bank Colliery, where it connects with Coronation Valley. Lastly, Arnot Valley extends south from north of Arnot, east of Arnot Colliery. These paleovalleys have played a significant role in controlling the distribution, thickness, and continuity of coal seams, particularly the No. 2 seam, resulting in complex facies relationships and irregular seam geometries across the coalfield (Hancox and Götz, 2014).

Except where the coal seams are tilted by dolerite intrusions, the coal seams and the surrounding strata are generally flat-lying to gently undulating, dipping regionally less than one degree towards the south and southeast (Hancox and Götz, 2014). The coal-bearing strata predominantly belong to the Vryheid Formation of the Ecca Group (Fig. 2). This formation comprises alluvium, multiple interbedded coal seams (No. 1 to 5), siltstones, limestones, sandstones, diamictite, and the pre-Karoo basement (Cadle and Cairncross, 1987; Hancox and Götz, 2014). Among the coal seams, No. 2 is the principal seam, notable for its thickness and high-quality coal, with an average thickness of approximately 7 m. It is extensively mined using both opencast and underground methods. The other seams such as No. 1, 3, 4 and 5 (from bottom to top) have average thicknesses of 2.15, 1, 2.5, and 1.8 m, respectively. Though thinner and generally of lower quality, these seams are also exploited throughout the coalfield.

The No. 1 seam is overlain by both siltstones and sandstones and underlain by siltstones, sandstones, diamictite and pre-Karoo basement rocks. The No. 2 seam is overlain by siltstones and interlaminated sandstone-siltstone layers and overlain by siltstones and sandstones. The no. 3 seam is overlain by siltstones and sandstones and underlain by thick sandstone layers. The No. 4 seam sits beneath a thick sandstone layer and above both siltstones and sandstones. Meanwhile, the No. 5 seam is enclosed between siltstones layers. The alluvium forms the uppermost layer, providing protection to the coal seams from erosion (Fig. 2).

3. Methods and materials

3.1. Sampling

The studied Storage Tailing Facility (STF) is rectangular ($1500\,m \times 500\,m$) in shape with varying height. It was established in 1987 and decommissioned in May 2002, with a total volume of 6, 400, 000 m^3. Currently, the facility is rehabilitated and well-maintained to manage environmental and safety risks, while restoring the land for sustainable

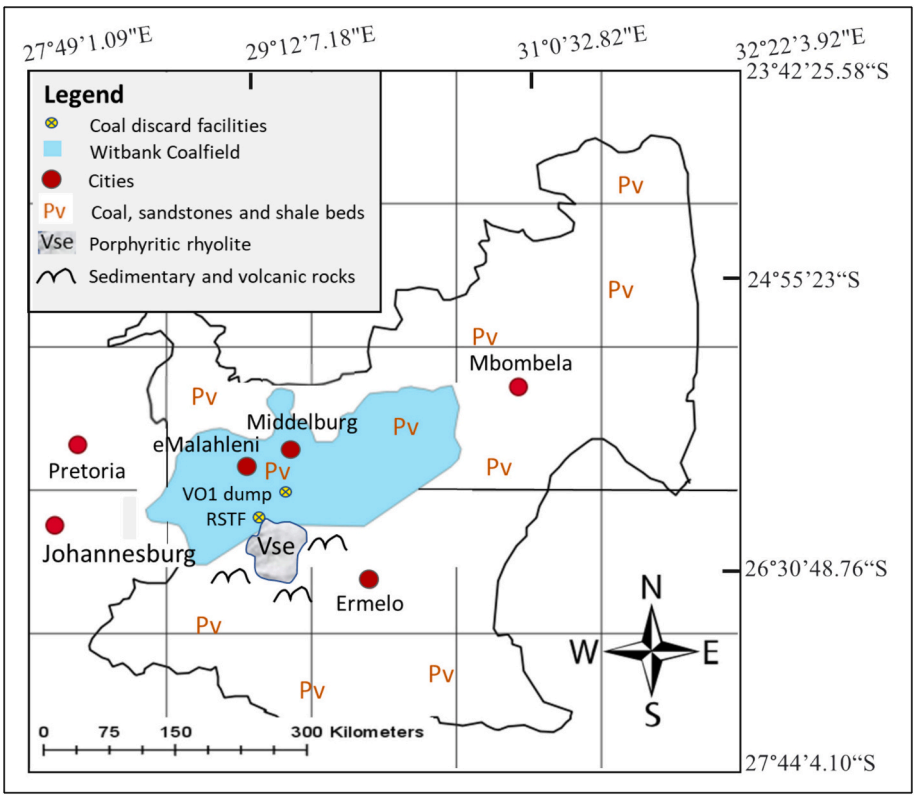

Fig. 1. Witbank Coalfield in the Mpumalanga province.

future use. A systematic drilling approach was employed, in which fourteen boreholes were drilled at evenly spaced intervals across the study area to ensure representative coverage of the variability in the coal discard material, as illustrated in Fig. 3. The spacing between boreholes was 200m, to ensure heterogeneity of the coal discard samples. Each borehole was drilled to a depth of 5 m using a truck-mounted drill rig. No drilling fluids were used during the drilling process. Upon completion, cores with a diameter of 80 mm were carefully recovered and labeled sequentially from STF001 to STF014, preserving their orientation and integrity. Each 5 m long core was then segmented in to five 1-m cores to facilitate detailed mineralogical and geochemical analyses. In total, seventy 1-m core samples were sealed, stored under appropriate conditions to prevent contamination, and labeled according to borehole number and depth interval (e.g., STF001 at 1 m to STF015 at 5 m).

3.2. Sample preparation

All samples were first air-dried and then crushed using a jaw crusher. The crushed material was split into representative samples using a sample splitter. From the splitter, two opposing representative samples were selected and further grounded using a milling machine to pass through 212, 75 and 50 μm test sieves. To prevent cross-contamination, especially from the finer size fractions, strict cleanliness protocols were followed. After processing each sample, the jaw crusher and splitter were cleaned with compressed air. The bowl and pestle of the end runner mill were thoroughly cleaned using a silica sand and wiped with a wiper roll. Additionally, each sieve utilized in the analysis was washed with water and dried using compressed air before the next sample was processed.

3.3. Coal quality assessment

3.3.1. TGA

The proximate parameters of coal discard samples (1 g) that passed through a 212 μm test sieve were determined according to ASTM D5142–09 standard (ASTM International, 2009) using TGA 701. The proximate analysis procedure involves multiple steps. Initially, nitrogen was employed for drying, starting at room temperature (around 20 °C) and gradually increasing to 107 °C at a heating rate of 8 °C/min, aiming to determine the inherent moisture content through mass loss measurements. Subsequently, volatile matter content was then assessed by monitoring mass loss within the temperature range of 107 to 950 °C. Following this, a combustion process in an oxygen environment was carried out, focusing on mass loss at 750 °C. The residual mass after these steps represented the total ash yield of the sample. Fixed carbon content was then calculated as 100 % minus the sum of moisture content, volatile matter content, and ash yield.

3.3.2. Bomb calorimeter

The calorific values of coal discard samples (1 g) that passed through a 212 μm test sieve were determined according to ASTM D5865–07 standard (ASTM International, 2007) using a Leco AC 500 bomb calorimeter. Initially, the bomb calorimeter was calibrated according to the manufacturer's guidelines, ensuring the cleanliness and integrity of all components. Simultaneously, a standard calibration was performed using 1 g of benzoic acid, thoroughly dried to eliminate any moisture. This calibration process involves igniting the benzoic acid in the calorimeter to record the temperature rise, repeated for reliability. Each sample, representing 1 g, was burnt in a closed vessel under an oxygen atmosphere at a high pressure of 3, 000 kPa, and the amount of heat released was measured. The temperature was maintained at 25 °C via circulating cooling water using a pump. The system uses an electronic thermometer with an accuracy of 0.0001 to measure the temperature every six seconds, with the results obtained within 4.5 to 7.5 min. Upon combustion, the bomb was rinsed, and the wash solution was treated to precipitate sulfate as barite. The mass of barite was only used to correct heat released from sulfur oxidation (based on approx. 36 KJ/mol H_2SO_4), which was subtracted from the gross calorific value to yield the

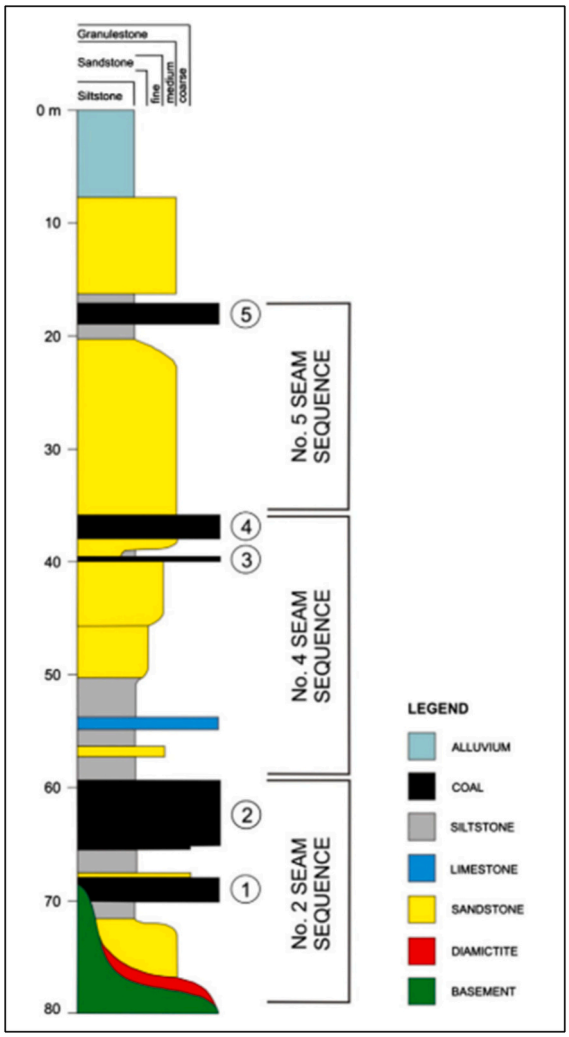

Fig. 2. Generalized stratigraphical sequence of the Vryheid Formation of the Ecca Group in the Witbank Coalfield (Hancox and Götz, 2014).

sulfur-corrected calorific values.

3.4. Mineralogical characterization

3.4.1. Fourier transform infrared spectroscopy (FTIR)

FTIR spectroscopy was used to analyze the molecular structure of the coal discard samples. For each analysis, 25 mg of powdered sample was carefully weighed and place in the compartment. The measurements were conducted using a Bruker Tensor II FTIR spectrometer coupled with an attenuated total reflectance (ATR) crystal, which allows direct analysis of powdered samples by measuring the evanescent wave that penetrates a few microns into the sample surface. Spectra were collected over a range of 4000 and 400 cm^{-1} with a resolution of 4 cm^{-1} and 32 scans. The data were processed using OPUS software to identify characteristic peaks corresponding to specific functional groups.

3.4.2. X-Ray diffraction (XRD)

XRD was utilized to determine the mineralogical composition and identify the crystalline phases present in the coal discard samples. For each analysis, 1.2 g of powered sample was prepared and loaded into the sample holder. The XRD patterns were recorded using a Bruker D2 Phaser diffractometer with Cu Kα radiation ($\lambda = 1.5406$ Å). Scans were performed over a range of 5° and 90° 2θ with a step of 0.02° and a counting of 2 s per step. The resulting data were analyzed using EVA software, which facilitates phase identification and quantification by comparing the measured peaks to entries in the ICDD PDF-4 database. It is important to note that XRD has a detection limit of approximately 0.5 wt%, therefore, mineral identifications below this threshold may be unreliable unless supported by complementary techniques such as SEM-EDS or TIMA.

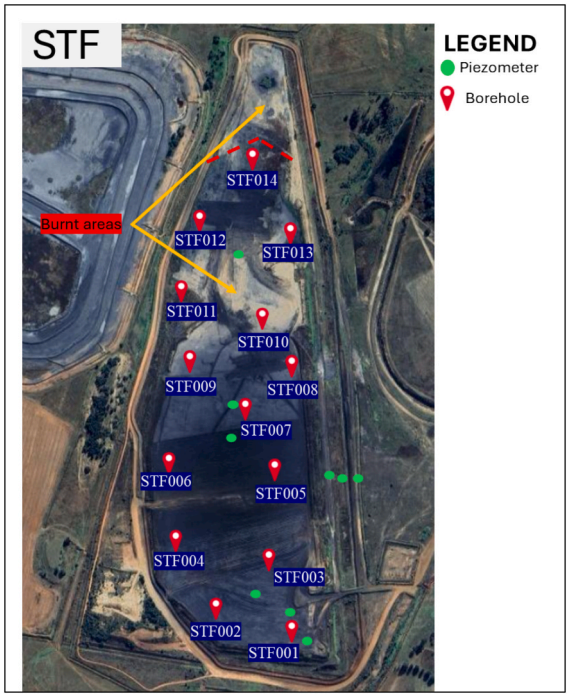

Fig. 3. STF layout with fourteen (14) evenly spaced sampling points, each is 200m apart.

3.4.3. Scanning electron microscope with energy dispersive spectroscopy (SEM-EDS)

SEM-EDS was used to examine the surface morphology and elemental composition of coal discard samples. For each analysis, approximately 0.5 g of the powdered sample was carefully prepared and mounted on aluminium stubs using carbon adhesive tape. The examinations were conducted using a ZEISS EVO MA10 SEM equipped with an Oxford Instruments Xplore30 silicon detector (SDD) for EDS analysis. The EDS system was operated using AztecLiveLite software (version 6.1). High-resolution SEM images were acquired at an accelerating voltage of 15 kV and a working distance of 10 mm to characterize the surface texture and particle morphology. EDS measurements were performed at an accelerating voltage of 20 kV and a working distance of 12.5 mm to optimize X-ray generation for quantitative and semi-quantitative analysis. Both spot analyses and area scans were used to identify and characterize the mineral phases present in the samples.

3.4.4. Tescan integrated mineral analyzer (TIMA)

TIMA was employed for automated mineralogical analysis, utilizing a field-emission scanning microscope (FE-SEM) combined with EDS to acquire high-resolution backscattered electron (BSE) images and elemental maps at 20 kV. For each analysis, 2 g of the powdered sample was carefully prepared. Polished, carbon-coated coal discard samples were analyzed with four EDS detectors and cross-referenced against a 5000+ mineral database for identification and quantification. The AutoLoader™ facilitated 24/7 unattended operation, enabling high-throughput analysis of 7 samples per day. TIMA is capable of accurately identifying mineral particles as small as approximately 1 μm, with a detection limit around 0.1 wt%. Nonetheless, mineral identifications below this threshold may be unreliable unless supported by other techniques such as SEM-EDS or XRD. Limitations of TIMA include

challenges in distinguishing chemically similar minerals, detecting particles smaller than 1 μm and its dependence on the quality and comprehensiveness of the reference database.

3.5. Geochemical characterization

The major oxides were determined by XRF using a PANalytical Axios X-ray fluorescence spectrometer equipped with a 4 kW Rh tube. The methodology followed was based on the procedure described by Cloete (2012). Trace elements were analyzed by ICP-MS after digesting a mixture of 250 mg of sample with 6 ml of 55 % HNO_3, 2 ml of 32 % HCl, 1 ml of 48 % HF, 0.5 ml of 30 % H_2O_2, and 1 ml of H_2O. The digestion process involved heating the solutions from 55 to 100 $^{\circ}C$ for 10 min, then from 100to 200 $^{\circ}C$ for 5 min, followed by holding at 200 $^{\circ}C$ for 35 min. After digestion, the vessels were cooled to room temperature with the stoppers closed. The resulting solutions were transferred to 50 ml tubes and diluted with deionized water. Prior to analysis, the solutions were filtered through 0.45 μm filters. Calibration was carried out using multi-element standards, while internal standards such as Rh and Re were employed to correct for matrix effects and instrumental drift. Certified reference materials were also analyzed to validate the accuracy of the method. Element concentrations were determined based on the calibration curves and reported in μg/g.

4. Results

4.1. Coal discard quality

The physicochemical properties of the coal discard samples are relatively homogeneous, though minor variations in certain parameters, such as ash yield (A) and fixed carbon (FC), are observed with depth, as illustrated in Fig. 4. The slight variation in fixed carbon is consistent with expectations for organic-rich samples, where depth-related changes in organic matter and mineral composition can affect fixed carbon content. Ash yield exhibits a slight increase at deeper depths, suggesting a higher mineral content in the deeper samples. Calorific value (CV) exhibits a modest decrease with depth, likely reflecting the combined effect of reduced organic matter and increased mineralization. This suggest that the energy potential of the coal discards diminishes slightly as depth increases. Notably, moisture and volatile matter contents remain stable throughout the depth profile, indicating preservation of these properties in the coal discard samples.

The contents of physicochemical properties of the coal discard samples from this study and the values reported in the literature on a dry basis, are presented in Table 1. The volatile matter content in the coal discards was higher than the average reported by the Department of Mineral Resources and Energy. In contrast, the ash yield was noticeably lower than the average. The fixed carbon content and calorific value of the coal discard samples were slightly higher than those typically found in the literature. According to the ASTM D388–99 classification standard, these coal discards, on a dry mineral matter basis fall into the High Volatile B Bituminous Coals category (ASTM International, 1999).

4.2. Mineralogy of coal discards

4.2.1. FTIR results

The FTIR spectra peaks of samples STF004 and STF009 (from 1 m to 5 m depth) were analyzed based on current literature (Painter et al., 1981; Fuller et al., 1982; Martin and Chao, 1988; Mastalerz and Bustin, 1993, 1996; Öztaş and Yürüm, 2000; Georgakopoulos, 2003; Oikonomopoulos et al., 2013; Xue et al., 2023). Prominent O—H stretching vibrations between 3600 and 3700 cm^{-1} (Fig. 5) suggest the presence of hydroxyl-bearing minerals, such as clay minerals including kaolinite, illite and muscovite. Aliphatic C—H stretches observed between 2800 and 3000 cm^{-1}, as well as between 1300 and 1400 cm^{-1}, indicate the presence of aliphatic hydrocarbons. The peaks between 1500 and 1600 cm^{-1} correspond to C═C aromatic rings, signifying aromatic hydrocarbons. C—O stretching near 1251.9 cm^{-1} suggests the presence of carbonyl groups and carbonate minerals such as calcite, dolomite, and ankerite. Saturated aliphatic C—C stretches at approximately 1029 cm^{-1} and C—Cl vibrations in the range of 690 and 760 cm^{-1}, consistently observed in all samples, reflect the complexity of the hydrocarbon structure present. The Al-OH peak at 912.17 cm^{-1} indicates aluminium hydroxyl-bearing minerals, such as clay minerals. Prominent Si—O and Si-O-Si peaks at 1007.60 and 535.30 cm^{-1}, respectively, reveal an abundance of silicate minerals. Lastly, sharp metal-oxygen (M-O) peaks at 466.71 cm^{-1}, consistently present across all samples, indicate metal-oxygen minerals such as hematite, magnetite, rutile and ilmenite.

4.2.2. XRD results

The XRD data show quartz and kaolinite dominate the minerals in Permian coal discards from the Witbank Coalfields, with minor amounts of calcite, dolomite, pyrite, magnetite, muscovite, and ankerite (Table 2). Quartz content generally increases with depth, while kaolinite

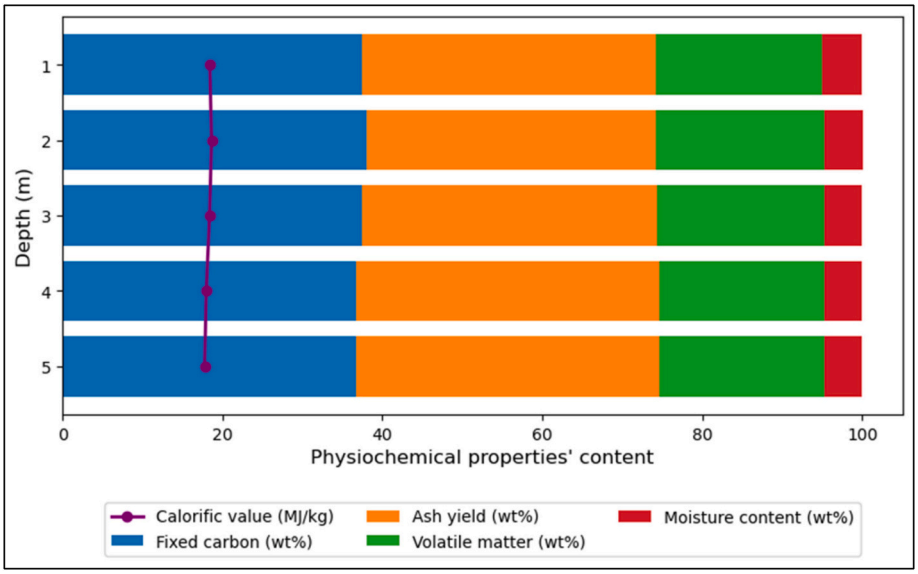

Fig. 4. The average content of physicochemical properties of coal discard samples per depth (m) on a whole rock basis.

Table 1
Proximate analysis (wt%) and calorific value (MJ/Kg) of STF coal discards across various depth on a dry basis.

Borehole ID	Depth (m)	M	VM	A	FC	CV
	1	0	24.21	40.07	35.72	16.2
	2	0	23.58	44.99	31.43	17.95
STF001	3	0	22.73	39.3	37.96	10.73
	4	0	23.71	35.71	40.57	18.19
	5	0	22.91	34.26	42.83	21.73
	1	0	24.02	36.8	39.18	18.05
	2	0	22.76	41.82	35.43	16.81
STF002	3	0	22.74	47.9	29.37	15.22
	4	0	23.08	43.49	33.42	16.88
	5	0	23.3	40.35	36.35	18.15
	1	0	24.97	35.34	39.68	18.3
	2	0	24.12	31.9	43.97	20.47
STF003	3	0	22.85	37.26	39.89	19.27
	4	0	23.85	32.62	43.53	20.66
	5	0	24.06	34.75	41.19	20.52
	1	0	24.32	31.39	44.29	19.25
	2	0	24.1	34.48	41.42	19.77
STF004	3	0	23.07	44.69	32.24	15.97
	4	0	22.95	48.41	28.64	14.75
	5	0	19.5	45.84	34.65	17.04
	1	0	23.22	30.25	46.52	21.16
	2	0	23.3	28.12	48.58	21.53
STF005	3	0	23.91	29.44	46.65	22.03
	4	0	24.25	27.43	48.32	23.33
	5	0	23.45	29.6	46.9	22.92
	1	0	17.67	57.74	24.59	0.12
	2	0	23.73	32.61	43.65	20.22
STF006	3	0	23.91	30.33	45.76	21.56
	4	0	22.64	33.07	44.29	21.55
	5	0	24.52	27.52	47.97	23.94
	1	0	23.64	31.99	44.36	20.96
	2	0	24.15	29.72	46.13	21.37
STF007	3	0	24.29	31.51	44.2	15.12
	4	0	22.79	35.81	41.4	19.92
	5	0	23.04	39.77	37.19	21.18
	1	0	24.14	32.19	43.68	19.87
	2	0	23.72	30.01	46.28	21.14
STF008	3	0	22.99	30.75	46.25	21.75
	4	0	23.99	28.61	47.4	23.76
	5	0	24.23	27.28	48.48	23.82
	1	0	24.22	34.22	41.56	18.89
	2	0	22.11	41.99	35.9	17.1
STF009	3	0	21.69	40.85	37.45	17.75
	4	0	16.66	55.38	27.95	13.65
	5	0	7.87	86.38	5.76	0.44
	1	0	23.98	33.95	42.05	19.5
	2	0	23.39	33.47	43.13	20.69
STF010	3	0	22.55	34.06	43.38	20.1
	4	0	22.59	35.54	41.87	20.44
	5	0	24.09	32.68	43.25	20.99
	1	0	23.34	34.09	42.57	19.17
	2	0	24.1	32.76	43.14	20.78
STF011	3	0	23.3	34.71	41.97	19.92
	4	0	23.98	31.38	44.65	22.51
	5	0	23.52	33.75	42.73	21.09
	1	0	23.94	36	40.06	17.6
	2	0	23.61	33.4	42.99	19.83
STF012	3	0	22.05	38.55	39.4	17.69
	4	0	23.38	37.62	39	19.98
	5	0	22.99	35.96	41.05	19.38
	1	0	23.51	37.26	39.22	18.64
	2	0	24.17	31.87	43.95	20.48
STF013	3	0	23.31	34.25	42.45	20.07
	4	0	22.78	35.15	42.08	21.21
	5	0	24.61	30.17	45.22	22.24
	1	0	22.2	39.74	38.05	18.77
	2	0	23.82	31.22	44.96	21.11
STF014	3	0	22.77	36.56	40.68	19.24
	4	0	22.71	41.25	36.03	19.08
	5	0	23.07	35.16	41.77	20.69
STF's average		0	22.98	36.43	40.59	19.33
Witbank's average (DMRE, 2001)		0	19	40	38	17

decreases, but other minerals remain fairly constant. Samples from boreholes STF006 at 1 m and STF009 at 5 m have notably high quartz content, likely due to localized input of quartz-rich material or selective disposal of quartz-rich waste during mining. Overall, these mineralogical trends appear driven more by the strategic layering of different waste materials during processing than by natural sedimentary processes, so no clear geological explanation fully accounts for the variations.

The high-intensity quartz peaks in Fig. 6 indicate its robust crystalline structure. The abundance and distribution of detrital quartz across the samples suggest that quartz has effectively resisted mechanical weathering (Wang et al., 2012). Similarly, pronounced kaolinite peaks are observed at 2θ values of approximately 12°, 25°, 38°, 39°, 45°, and 63° as shown in Fig. 6. Kaolinite forms through various processes across different geological environments, such as crystallization from solution, replacement of pre-existing minerals, crystallization from colloidal gels, and weathering of both layered and non-layered silicates (Parham, 1969). Specifically, kaolinite forms from intermediate phases that emerged on the felspar surfaces during weathering in the form of tiny bumps and tempered projections (Parham, 1969). For instance, in the Datong Coalfield, the presence of platy kaolinite in coal has been attributed to feldspar weathering (Liu et al., 2021a). Its distinctive layered structure facilitates the adsorption of trace elements onto its surface and allows potential interactions with organic matter.

The identification of muscovite in the sample indicates the stability of mica phases during sedimentary processes and reflects contributions from either metamorphic or igneous source rocks with relatively limited alteration. A minor peak at approximately 35.5° 2θ corresponds to magnetite (Fig. 6). This iron-bearing phase, though present in small amounts, indicates localized oxidizing conditions during coal formation and is often found as inclusion within oxidized zones of coal (Wagner et al., 2019). Its occurrence also suggests detrital input from igneous or metamorphic rocks. Pyrite was detected as a less abundant phase, evidenced by a subtle peak near 42° 2θ, confirming the presence of sulfide minerals. This supports the interpretation that coal formation occurred under anaerobic conditions through both syngenetic and epigenetic processes (Li et al., 2016).

Carbonate minerals such as calcite, dolomite and minor ankerite, were also present, indicating a significant carbonate fraction with both syngenetic and epigenetic origin (Wang, 2017). The calcite peak appears at 29° 2θ, while dolomite and ankerite peaks, which overlap, occur around at 31° 2θ (Fig. 6). The presence of calcite suggests the influence of carbonic-rich fluids from marine or lacustrine environment as well as possible contributions from biological activity such as microbial processes and shell fragments (Vassilev and Vassileva, 1996). The coexistence of dolomite and ankerite reflects varying fluids chemistries; dolomite forms though precipitation from Mg-rich fluids, whereas ankerite results from fluids enriched in Mg, Mn and Fe.

4.2.3. *SEM-EDS results*

The SEM-EDS focuses on the morphology of minerals present in the coal discards. Based on the XRD data, it has been observed that all the coal discards have similar mineralogical compositions despite different depth ranges. Hence, there was no comparison between the types of minerals present at each depth.

4.2.3.1. Silicate minerals. Silicate minerals are typical constituents of coal mineral matter. They originate from detrital input, authigenic formation, and volcanic ash during diagenesis (Dai and Chou, 2007). In the Witbank Coalfield, the principal silicate minerals are quartz and kaolinite, accompanied by smaller proportions of muscovite, illite and montmorillonite. The angular to subangular quartz grains illustrated in Fig. 7a indicate a detrital input, with limited transport and minimal mechanical weathering. Fig. 7b illustrates fine-grained, platy, and flaky montmorillonite aggregates, indicative of low-grade digenesis typically

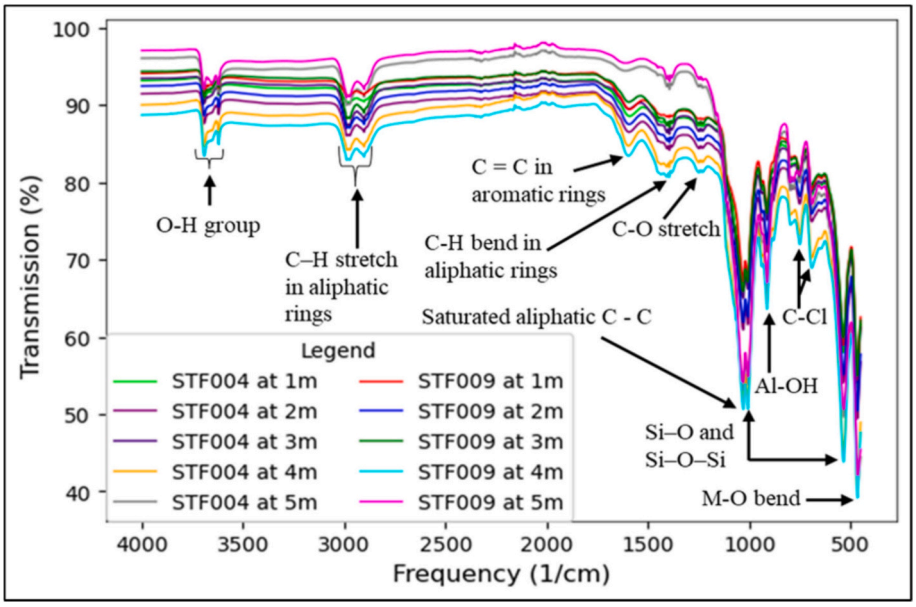

Fig. 5. The FTIR spectra for selected coal discard samples at different depths.

associated with early authigenesis or weathering-derived input. The compacted and irregularly edged kaolinite with a blocky texture depicted in Fig. 7e reflects a more mature, diagenetically transformed phase, pointing to intense weathering of intermediate phases or feldspar. Ultimately, the platy and angular muscovite grain surrounded by fine-grained materials in Fig. 8f implied low-energy depositional environment during coal formation.

4.2.3.2. Carbonate minerals. Calcite, siderite, and dolomite are typical carbonate minerals present in coal mineral matter. Calcite and dolomite originate from hydrothermal fluids and groundwater (Shao et al., 2022). Siderite minerals with Fe^{+2} typically form in a low-oxygen environment (Dai et al., 2015). Small, euhedral, elongated, and fragmented crystals of siderite, as illustrated in Fig. 8b, suggest minimal transportation, early diagenetic stage, and intense mechanical weathering. In contrast, anhedral fragmented siderite crystals as illustrated in Fig. 8d indicate intense transportation and weathering.

4.2.3.3. Sulfide and sulfate minerals. Sulfide minerals formed in coal during syngenetic and epigenetic processes. Small subhedral crystals of pyrrhotite, as illustrated in Fig. 9a, reflect the decomposition of pyrite during coal combustion. Pyrite forms in a low-oxygen environment where crystal growth is limited, due to small space or chemical precipitation. As shown in Fig. 9b, barite appears as a well-defined tabular, plate-like crystal with clear angular edges, suggesting minimal alteration, while in Fig. 9d appears as a more massive crystal form with a rough surface, indicating intense weathering.

4.2.3.4. Other minerals. These are oxide minerals such as zircon, hematite, Ti-hematite, and ilmenite. The presence of magnetite, Ti-hematite, and ilmenite suggests that coal seams were subjected to an oxidizing condition in a micro-environment. Ti-hematite appears as an elongated, tabular crystal form as shown in Fig. 10a, derived from mafic or heavy minerals (Farjana et al., 2018). Its rough surface and sharp edges suggest it went through an alteration in situ environment. The sub-rounded grain of magnetite with some patches of organic matter on the surface, as illustrated in Fig. 10b, indicates that the magnetite was transported by water and deposited in an oxidizing environment. The platy-like crystal of ilmenite with some slickenlines and small inclusion of organic matter on the surface, as illustrated in Fig. 10e, suggests the presence of faults caused by tectonic or volcanic activities. Subhedral crystal of ilmenite as shown in Fig. 10f suggests that ilmenite formed under high-temperature and high-pressure conditions in a magmatic environment. A well-developed, euhedral crystal form of zircon with tetragonal prismatic structure, as shown in Fig. 10c, shows that detrital zircon resisted weathering.

4.2.4. TIMA results

TIMA was employed to complement the XRD and SEM-EDS data by cross-validating the mineral phases detected by those methods. Only two samples (STF009 at depth of 2 m and STF009 at depth of 4 m) were selected for analysis, as all coal discard samples exhibited similar mineralogical composition regardless of depth. Quartz and kaolinite were the predominant minerals across all samples. These results align with the semi-quantitative XRD data, which similarly identified quartz and kaolinite as the major mineral phases. Quartz content increases with depth, while kaolinite declined correspondingly. The STF009 sample at 2 m depth was dominated by quartz, kaolinite, pyrite, calcite, fusinite, vitrinite, and siderite. In contrast, the 4 m depth sample predominantly contained quartz, kaolinite, fusinite and microcline.

As illustrated in Fig. 11b, small illite phases were observed alongside with muscovite at the edges of microcline grains, suggesting that illite is formed under hydrothermal or low-grade metamorphism conditions (Aja, 2019). Siderite particles were dispersed among quartz, clay minerals, and organic matter, and were found associated with calcite and dolomite, indicating precipitation of carbonate minerals during coal formation. Additionally, small siderite particles occurred within pyrite, implying iron mineralization under sulfur-rich conditions. Dolomite particles embedded within calcite in Fig. 11a and b; align with SEM-EDS observations. This textural relationship results from incomplete dissolution of calcite followed by precipitation and substitution of Ca by Mg in a shallow marine environment (Querol et al., 2001). In Fig. 11b, pyrite surfaces were covered by small particles of kaolinite, dolomite, and to a lesser extent, fusinite and quartz. The presence of ilmenite, fusinite (high carbon content), dolomite and kaolinite on pyrite implies a complex geological history, where these minerals were deposited after pyrite crystallization. Fig. 11a and b also show gypsum adjacent to pyrite, suggesting that pyrite oxidation occurred, producing sulfate ions that reacted with calcium to form gypsum. Furthermore, the presence of small calcite and dolomite particles on gypsum surfaces (Fig. 11b) indicates incomplete transformation of carbonate minerals into gypsum.

Table 2
Semi-quantitative mineral phase composition (wt%) of boreholes STF001–014 identified by X-ray diffraction across various depth from 1 to 5 m on a whole rock basis.

Borehole ID	Depth (m)	Q	K	D	C	A	M	Mu	P
	1	41.11	24	9.35	14.49	1.95	3.31	2.88	2.43
	2	40.91	24.02	9.25	14.36	1.84	3.06	2.88	2.25
STF001	3	45.13	19.91	9.13	14.07	1.68	3.16	3.12	2.33
	4	46.7	18.07	9.25	14.4	1.93	3.54	2.67	2.6
	5	46.72	18.34	9.35	14.54	1.96	3.19	2.74	2.34
	1	42.9	23.45	9.35	14.66	1.93	2.47	2.74	1.82
	2	39.76	24.33	9.43	14.82	2.16	3.4	2.95	2.5
STF002	3	40.15	18.35	9.43	14.72	2.54	6.37	2.98	4.69
	4	42.45	17.77	9.48	14.88	2.5	5.48	2.84	4.03
	5	45.69	16.47	9.33	14.49	2.12	4.48	2.77	3.29
	1	44.54	23.48	9.17	14.26	1.61	1.93	2.75	1.42
	2	46.24	22.7	9.09	14.11	1.5	1.78	2.57	1.31
STF003	3	50.47	14.64	9.09	14.06	1.74	3.58	2.8	2.63
	4	48.96	17.74	9.18	14.27	1.77	2.98	2.35	2.19
	5	46.14	15.55	9.34	14.5	2.24	5.24	2.55	3.85
	1	45.54	17.68	9.64	15.28	2.41	3.25	3.28	2.39
	2	52.3	14.46	9.29	14.52	1.84	2.4	2.52	1.77
STF004	3	50.86	12.33	9.63	15.27	2.43	3.42	2.95	2.51
	4	45.78	12.03	9.89	15.83	3.04	5.37	3.11	3.95
	5	56.28	13.2	8.71	13.31	1.04	1.84	3.6	1.35
	1	40.22	29.26	8.95	13.79	1.23	1.24	2.51	1.91
	2	47.78	25.33	8.61	13.13	0.77	0.74	1.64	1.54
STF005	3	51.93	18.65	8.84	13.59	1.09	1.03	2.41	1.76
	4	51.56	18.24	8.96	13.81	1.32	1.72	2.17	1.27
	5	53.34	16.38	8.93	13.78	1.23	1.26	2.37	1.93
	1	64.77	13.02	8.65	6.17	1.12	2.89	2.43	1.13
	2	53.16	24.63	9.05	6.93	1.42	1.89	0.56	1.39
STF006	3	54.07	24.69	8.95	6.81	1.27	1.38	0.57	1.01
	4	54.09	23.94	9	6.89	1.4	1.96	0.64	1.44
	5	55.17	23.98	8.94	6.75	1.25	1.5	0.42	1.1
	1	44.39	23.72	9.08	13.99	1.49	2.14	2.83	1.57
	2	47.32	22.49	9	13.91	1.35	1.56	2.52	1.14
STF007	3	46.19	22.49	9.05	14.02	1.48	1.99	2.53	1.46
	4	47.69	17.14	9.23	14.34	1.86	3.26	2.93	2.39
	5	48.17	21.87	8.91	13.74	1.33	2.07	1.8	1.52
	1	45.89	23.6	8.95	13.76	1.21	1.2	2.8	1.88
	2	44.22	25.35	9.04	13.98	1.39	1.57	2.5	1.15
STF008	3	44.81	24.92	9	13.92	1.34	1.39	2.39	1.02
	4	45.24	25.13	8.96	13.82	1.28	1.44	2.45	1.06
	5	48.24	21.69	8.98	13.85	1.32	1.57	2.35	1.16
	1	43.3	21.79	9.87	15.89	2.56	1.84	2.95	1.36
	2	41.29	21.97	9.21	14.24	1.97	4.47	3	3.29
STF009	3	43.25	22	9.14	14.14	1.76	3.43	3.03	2.52
	4	59.66	10.14	8.66	13.21	0.95	1.59	4.24	1.17
	5	92.7	1.58	nd	nd	nd	nd	5.2	nd
	1	44.42	23.23	9.14	14.14	1.56	2.02	2.7	1.48
	2	44.87	22.74	9.26	14.47	1.76	2.06	2.58	1.52
STF010	3	46.8	23.08	8.86	13.63	1.11	1.06	2.44	1.78
	4	45.57	21.2	9.23	14.4	1.79	2.57	2.45	1.89
	5	45.8	20.42	9.25	14.41	1.82	2.78	2.51	2.04
	1	44.24	23.98	9.09	14.06	1.51	2	2.89	1.47
	2	45.09	23.08	9.1	14.08	1.54	2.13	2.67	1.57
STF011	3	44.02	23.1	9.18	14.31	1.69	2.26	2.67	1.66
	4	43.05	25.5	9.07	14.04	1.48	1.93	2.53	1.42
	5	46.36	21.01	9.08	14.07	1.58	2.45	2.66	1.8
	1	42.61	24.5	9.24	14.31	1.69	2.29	3.01	1.68
	2	43.87	23.22	9.2	14.24	1.69	2.53	2.7	1.86
STF012	3	44.05	23.74	9.11	14.12	1.57	2.2	2.82	1.62
	4	41.78	23.37	9.37	14.7	2.02	2.92	2.72	2.15
	5	43.8	23.56	8.97	13.82	1.47	2.73	2.79	2.01
	1	41.96	23.9	9.54	15.08	2.09	1.88	2.86	1.38
	2	44.82	22.91	9.09	14.01	1.43	1.66	2.63	1.22
STF013	3	44.33	23.55	9.1	14.05	1.53	2.19	2.79	1.61
	4	42.59	23.12	9.12	14.1	1.71	3.22	2.67	2.37
	5	47.15	21.77	9.03	13.99	1.44	1.86	2.36	1.37
	1	44.81	24.12	9.02	13.92	1.39	1.78	3.18	1.31
	2	45.86	22.4	9.1	14.04	1.49	1.96	2.5	1.44
STF014	3	48.08	19.92	9.09	14.09	1.56	2.25	2.88	1.65
	4	47.11	18.65	9.33	14.62	1.95	2.8	2.92	2.06
	5	50.2	17.12	8.94	13.74	1.46	2.95	2.56	2.17

Q-quartz, K-kaolinite, C-calcite, D-dolomite, A-ankerite, M-magnetite, Mu-muscovite, P-pyrite and nd – not detected.

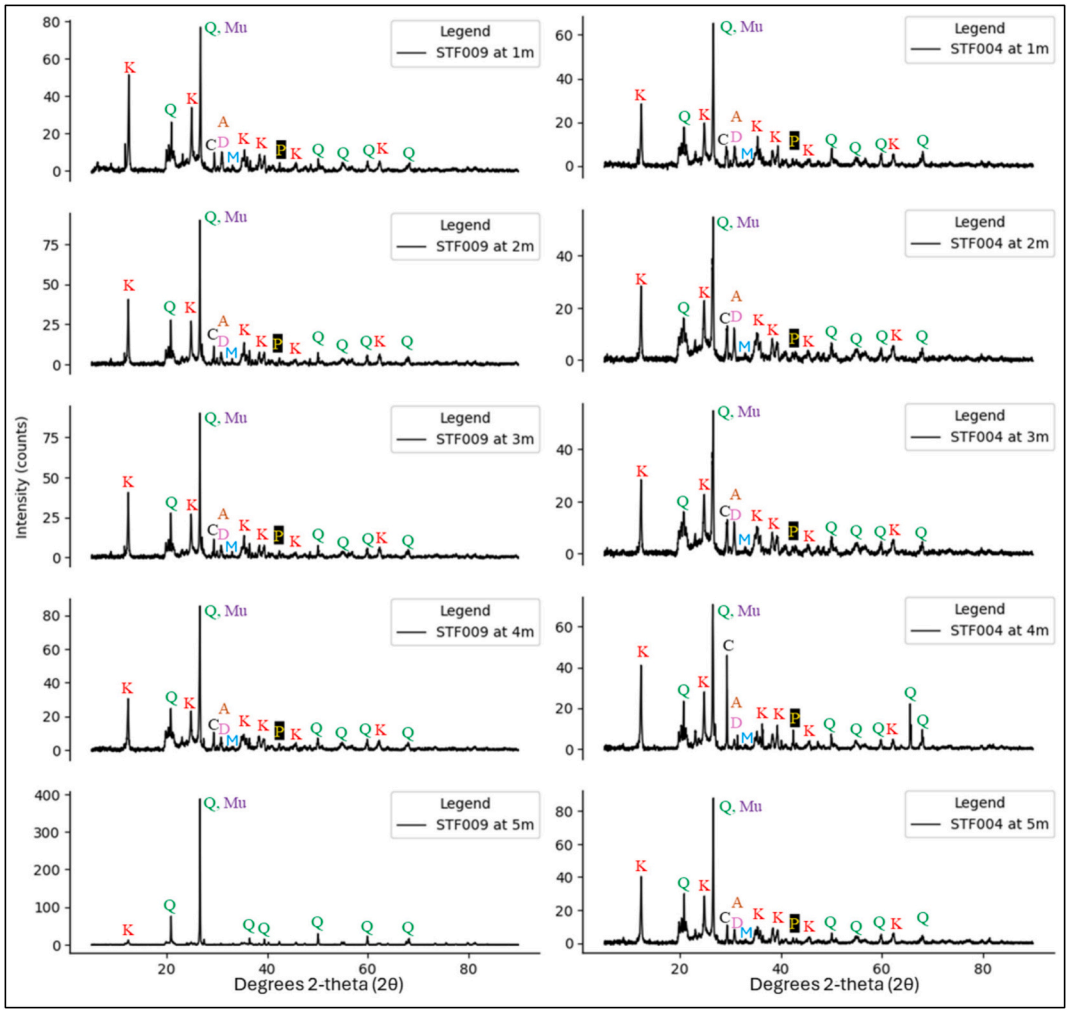

Fig. 6. XRD data for coal discards samples at various depths, Q-quartz, K-kaolinite, Mu-muscovite, C-calcite, D-dolomite, M-magnetite, P-pyrite, and A-ankerite.

4.3. Geochemistry of coal discards

4.3.1. Major oxides

The main components of the coal discards in the Witbank Coalfield are SiO_2 and Al_2O_3, which together account for approximately 76 % of the major oxides present in these samples (Table 3). The weighted averages of SiO_2 and Al_2O_3 are 20.15 and 9.33 wt%, respectively. Notably, the Al_2O_3 content falls below 37 %, the standard criterion for high Al-bearing coal (Sun et al., 2022). Concentration coefficients (CC) for the coal discards were determined by dividing the average oxide concentrations by the corresponding averages reported for South African coals, based on the data from Pinetown (2007), Netshitungulwana et al. (2022), Biswas et al. (2024), Modiba and Wagner (2024). The resulting CCs values are: 0.33 for SiO_2, 0.60 for TiO_2, 0.45 for Al_2O_3, 0.72 for Fe_2O_3, 1 for MnO, 0.71 for MgO, 1.06 for CaO, 0.78 for Na_2O, 0.48 for K_2O and 1.1 for P_2O_5, as illustrated in Fig. 12. Chromium oxides were generally excluded from this analysis owing to their consistently low concentrations.

These CC values indicate a depletion of SiO_2 and Al_2O_3 in the coal discard samples relative to South African coal averages, suggesting a lower abundance of silicate minerals such as quartz and clay minerals. This observation is consistent with TIMA data, which also show decreased silicate mineral content across various depths. In contrast, CaO and P_2O_5 exhibit slight enrichment, indicating the presence of carbonate and phosphate minerals such as calcite, ankerite, apatite, and dolomite. The relative depletion of K_2O may reflect the limited presence of potassium-bearing minerals such as muscovite, which is consistent with TIMA and XRD data showing reduced muscovite content throughout the coal discard samples. Similarly, notable depletion of TiO_2, Fe_2O_3, MgO, and Na_2O reflects the limited presence of Ti-, Fe-, Mg-, Na-bearing minerals such as anatase, pyrite, montmorillonite, ankerite, hematite, ilmenite, and albite. These findings align well with TIMA data showing reduced content of these minerals. Overall, the geochemical composition observed in these samples corresponds with regional coal characteristics reported in previous studies, offering valuable insights into the depositional environment and diagenetic processes that have influenced the Witbank Coalfield coal seams.

4.3.2. Trace elements

The average concentrations of trace elements analyzed by ICP-MS are summarized in Table 4. The analysis includes a comprehensive list of elements such as Li, Be, Sc, Co, Ni, Cu, Zn, Ga, Rb, Sr, Y, Zr, Nb, Mo, Ba, La, Ce, Nd, and Pb. However, some REEs and other elements were consistently below the detection limit in all samples and are therefore excluded from the data presentation. The focus on Ga, Sr, Zr and Ba stems from their prominence as the abundant elements in South African coal discards, exhibiting notably higher ppm values compared to other detected elements (Maphoso et al., 2024). To ensure clarity and relevance, only those elements that were reliably detected are reported.

The average Ba concentration was 960.85 μg/g, which is approximately four times higher than the Ba cut-off grade of 150 μg/g, (Ketris and Yudovich, 2009). Sr had an average concentration of 344.94 μg/g.

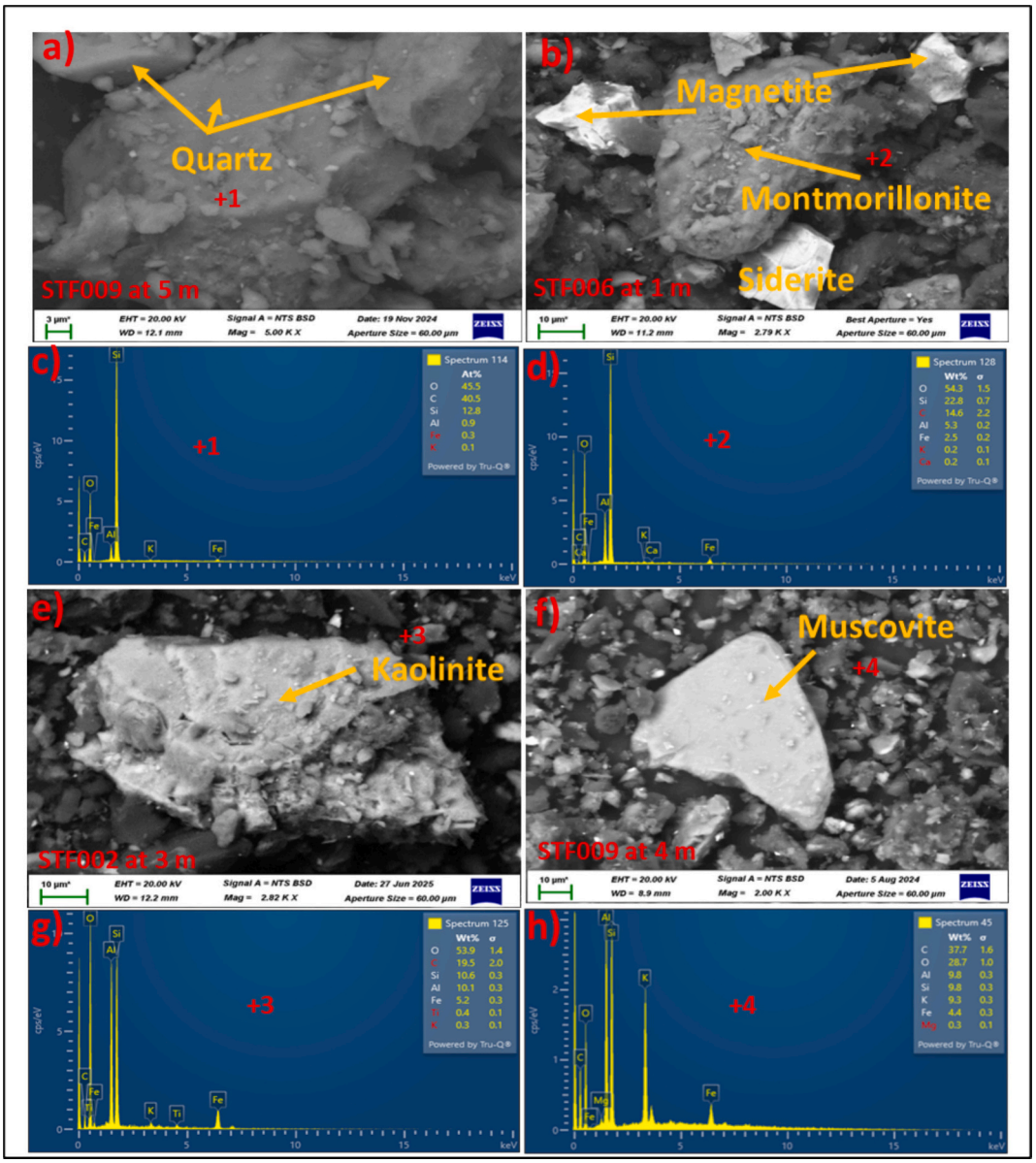

Fig. 7. a) angular to subangular grains of quartz, b) fine-grained, platy, and flaky montmorillonite aggregate, c) EDS spectrum for point +1, d) EDS spectrum for point +2, e) irregular edged kaolinite particle with a blocky texture, f) platy and angular muscovite grain with a smooth texture, g) EDS spectrum for point +3, and f) EDS spectrum for point +4.

Zr averaged 495.39 μg/g significantly exceeding the world average concentrations in coal, which are reported as 35 μg/g for low-rank coals and 36 μg/g for hard coals (Ketris and Yudovich, 2009). For comparison, average Zr concentration have been reported as 27 μg/g in U.S. coals (Orem and Finkelman, 2005) and 89.5 μg/g in Chinese coals (Dai et al., 2012a). Ga averaged 141.07 μg/g, notably higher than its cut-off grade of 30 μg/g (Dai et al., 2006a). Concentration coefficients (CC) were determined by diving the average concentration of each trace element in the coal discards by the corresponding global averages for hard coals provided by Dai et al. (2015a). As shown in Fig. 13, the Witbank Coalfield coal discards are significantly enriched in Ba, Zr and Ga (CC > 5); moderately enriched in Sr, Li, Co, Ni, Cu, Zn, Pb, Rb and Nb (2 < CC < 5); slightly enriched in Sc (1.2 < CC < 2); depleted in Y (0.5 < CC < 1.2) and significantly depleted in La, Ce and Nd (CC < 0.5) when compared to hard coals around the world (Ketris and Yudovich, 2009). Notably, the concentrations of Mo and Be were comparable to global averages for hard coals. Overall, the studied coal discards are characterized by enrichments of Ba, Zr, Ga, Sr, Li, Co, Ni, Cu, Zn, Pb, Rb, and Nb.

5. Discussion

5.1. Vertical distribution of Major oxides and Ga, Sr, Zr and Ba

The spatial distribution of elements in the coal discard dump was examined along the vertical profile. One particularly observation is that coal discards at shallower depths are more likely to have undergone leaching, oxidation, erosion, weathering and spontaneous combustion, whereas those at greater depths tend to be relatively fresh (Vo et al., 2022). As shown in Fig. 14, the averages of major and trace elements were calculated as the arithmetic mean of samples collected at each depth. Across the different depths, major oxides exhibited only minor fluctuations, indicating a relatively uniform geochemical composition and consistent mineralogy. In contrast, trace elements displayed moderate geochemical mobility with depth.

Specifically, Ba concentration increased with depth up to 4 m before declining; Ga showed a gradual increased until 4 m, then decreased; Sr generally decreased with depth but spiked at 4 m; and Zr remained

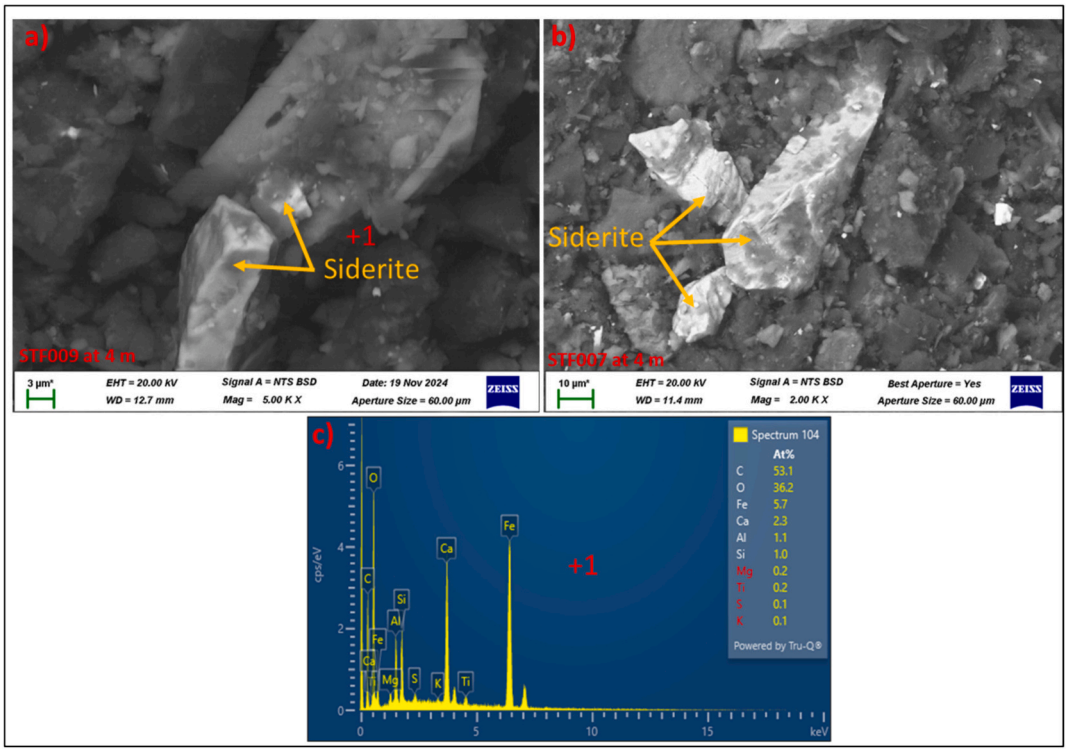

Fig. 8. a) Small, euhedral, elongated, and fragmented crystals of siderite and b) anhedral, fragmented siderite crystals.

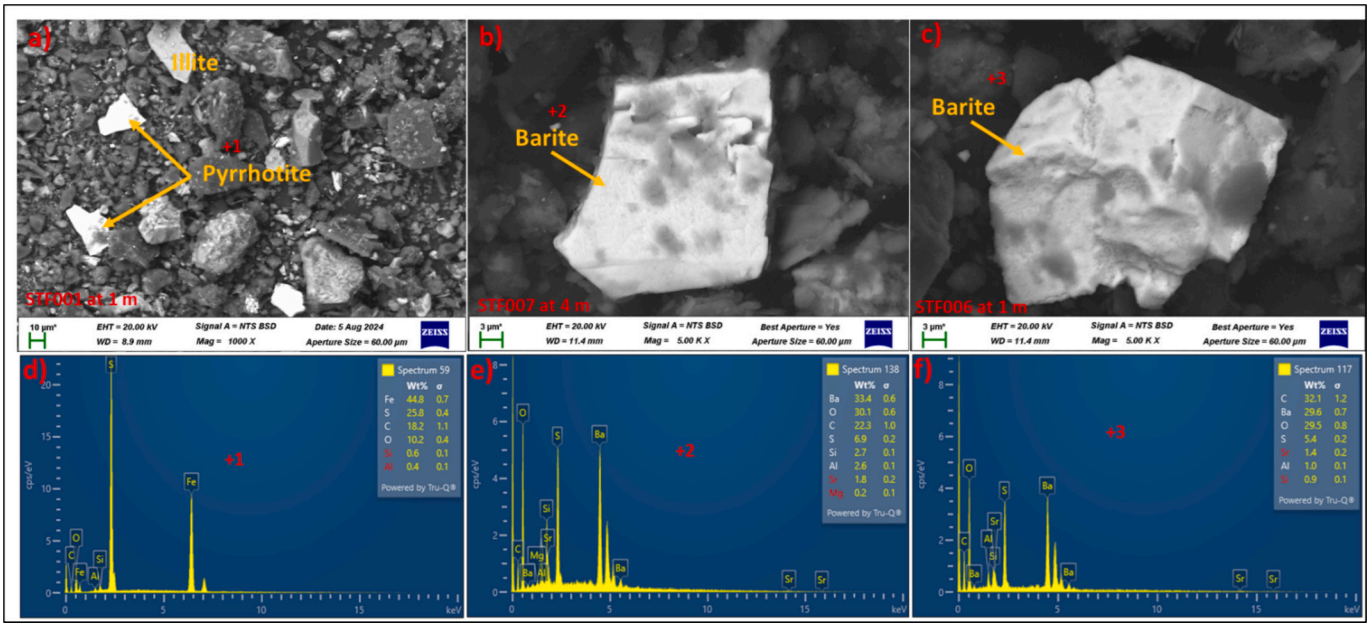

Fig. 9. a) small subhedral crystals of pyrrhotite, b) tabular, plate-like and euhedral barite crystal with clear angular edges, c) massive subhedral crystal of barite with rough surface, d) EDS spectrum for point +1, e) EDS spectrum for point +2 and f) EDS spectrum for point +3.

mostly stable with a slight increase at 5 m. These patterns suggest that trace elements tend to concentrate at deeper levels, possibly transported by water. CaO was depleted at 5 m, indicating the presence of acidic groundwater that likely dissolved calcite (Liu et al., 2018). The SiO_2/Al_2O_3 ratios measure were 2.18 at 1 m, 2.00 at 2 m, 2.05 at 3 m, 2.22 at 4 m, and 2.36 at 5 m, slightly higher than the theoretical ratio of 1.18 for pure kaolinite (Zheng et al., 2016). This supports the interpretation that quartz is the dominant mineral, followed by kaolinite, consistent with XRD and TIMA data. Additionally, SiO_2 is also present in other silicate minerals with high Si concentration such as illite, muscovite, smectite layer and zircon.

5.2. *Modes of occurrence of Ga, Sr, Zr and Ba*

The mode of occurrence of elements in coal results from various processes during peat deposition, followed by geological processes during diagenesis and epigenesis. It provides valuable insights into the origin of the elements, the geochemical processes undergone by the

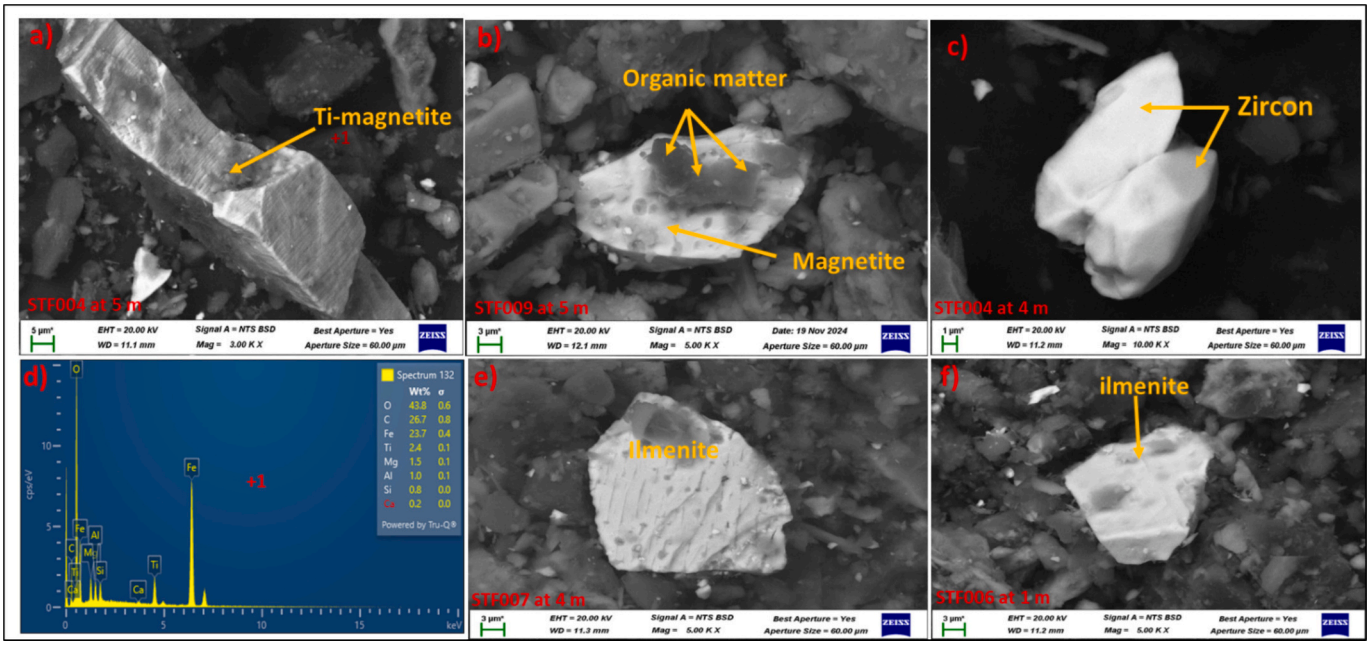

Fig. 10. a) Elongated tabular crystal of ilmenite, b) sub-rounded grain of magnetite with some patches of organic matter, c) prismatic crystals of zircon, d) EDS spectrum for point +1, e) anhedral ilmenite crystal with slickenslines, and f) subhedral crystal of ilmenite.

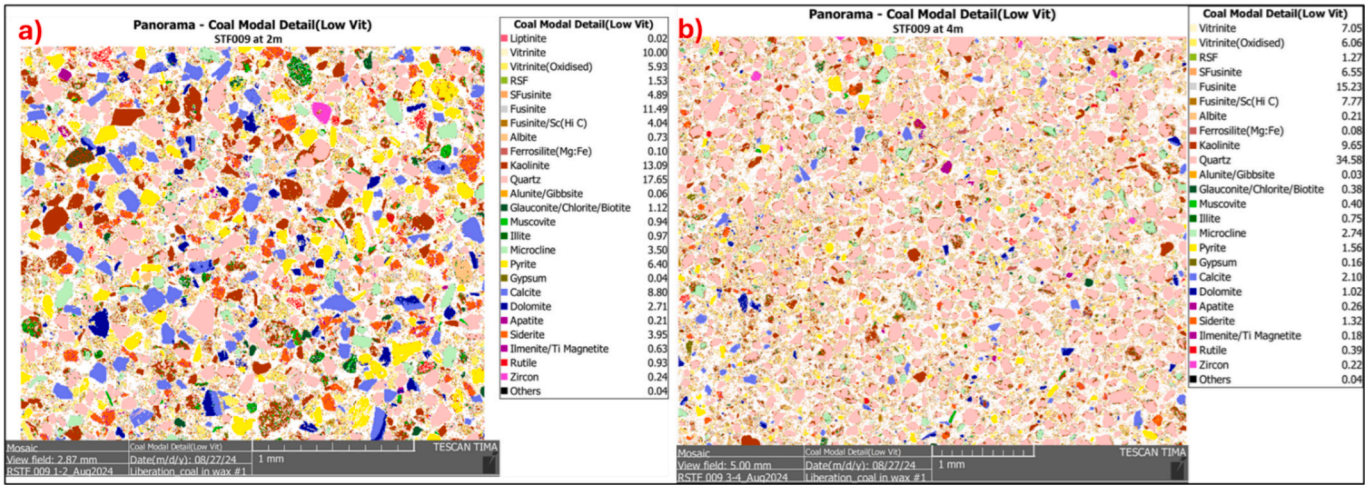

Fig. 11. TIMA images and quantitative data showing mineral and organic matter contents at various depths.

Table 3
Average concentration of major oxides (wt%) at various depths on a whole rock basis.

Depth (m)	SiO2	TiO2	Al2O3	Fe2O3	MnO	MgO	CaO	Na2O	K2O	P2O5	LOI
1	21.69	0.63	9.97	3.19	0.04	0.91	3.46	0.19	0.53	0.24	59.13
2	18.32	0.62	9.16	3.3	0.03	0.89	3.15	0.16	0.41	0.23	63.72
3	19.5	0.65	9.51	3.76	0.04	0.86	3.14	0.18	0.49	0.23	61.63
4	20.26	0.66	9.13	4.3	0.04	0.88	3.41	0.18	0.47	0.24	60.42
5	21.41	0.66	9.06	4.14	0.04	0.84	2.79	0.18	0.54	0.22	60.1

parent peat and coal, and crucially, how the elements will behave during coal cleaning, utilization, leaching, and disposal (Orem and Finkelman, 2005; Finkelman et al., 2019; Dai et al., 2021). Indirect methods, such as statistical methods, have been widely used to investigate the modes of occurrence of elements in coal. However, these methods have inherent uncertainties due to their purely statistical nature and lack of mineralogical evidence. Recent studies recommend complementing statistical analyses with at least one direct method such as SEM-EDS or EPMA, to address these limitations (Orem and Finkelman, 2005; Dai et al., 2021). Accordingly, this study combines the statistical method with direct methods such as SEM-EDS, XRD, and TIMA, to provide a more robust and comprehensive understanding of the elemental occurrence.

5.2.1. Ga

Ga typically isomorphically substitutes for Al in Al-bearing minerals owing to their similar electronegativity, ionic radii, and charges (Wang

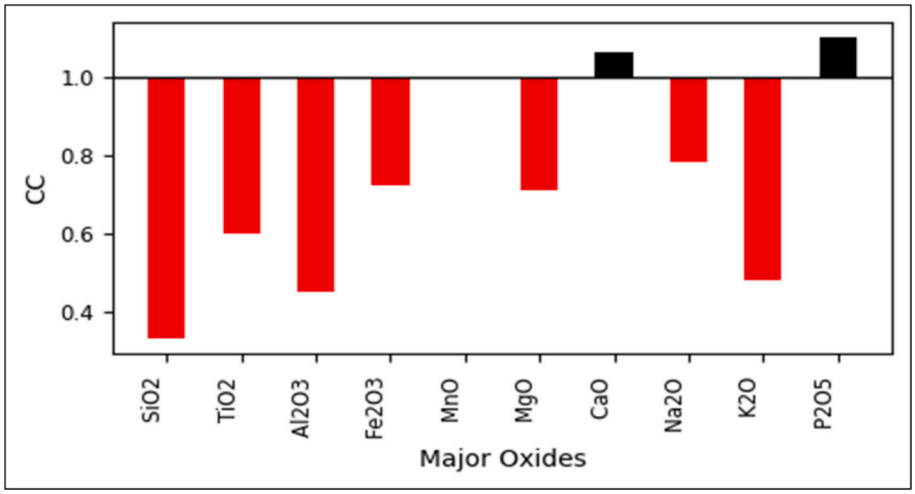

Fig. 12. The concentration coefficients of major oxides in the coal discards of the Witbank Coalfield compared to the average concentration of major oxides in South African coals (Pinetown, 2007; Netshitungulwana et al., 2022; Biswas et al., 2024; Modiba and Wagner, 2024).

et al., 2011). However, Ga has multiple modes of occurrence in coals. For instance, in the high-volatile bituminous coals of the Jungar Coalfield, Ga is primarily hosted by collotelinite maceral (Jiu et al., 2023), whereas in the medium-volatile bituminous coals of the Muli Coalfield, it is predominantly associated with kaolinite (Shao et al., 2018). Although some Ga-bearing minerals such as boehmite and goyazite were not detected by SEM-EDS, XRD and TIMA except for kaolinite, most studies reported that Ga primarily occurs in Al-bearing minerals, especially kaolinite (Wang et al., 2011; Shao et al., 2018; Zhao et al., 2019), as well as boehmite (Dai et al., 2006, 2006a; Wang et al., 2011; Shao et al., 2018) and goyazite (Dai et al., 2012; Zhao et al., 2019). This study showed that kaolinite is the second most abundant mineral in coal discards. Given the significantly elevated Ga concentration (CC $>$ 5) compared to averages reported for most hard coals around the world, it is reasonable to infer that kaolinite and organic matter are the primary carriers of Ga in these samples. However, this inference should be considered with caution due to limited direct mineralogical evidence.

5.2.2. Sr

Sr occurs in organic matter in low-rank coals and in calcite in hard coals (Swaine, 1990). Previous studies have reported that Sr occurs in minerals such as celestine, clay minerals, gypsum, strontianite, barite, crandallite, gorceixite and goyazite. To a lesser extent, Sr has also been identified in clinoptilolite, heulandite (Swaine, 1990; Dai et al., 2013, 2015; Spiro et al., 2019) and svanbergite (Li et al., 2016). A statistical correlation study revealed that leached Sr shows a strong positive correlation with both low-Ge and high-Ge coals (Liu et al., 2021). The Sr concentration is slightly enriched (2 $<$ CC $<$ 5) compared to the average levels for most coals worldwide. SEM-EDS analyses show that Sr is present in barite, which aligns with previous findings that sulfate minerals are frequent carriers of Sr in coal (Karayiğit et al., 2000). As illustrated in Fig. 15a and b, Sr exhibits a weak positive correlation with P_2O_5 and CaO, respectively. This suggests that Sr isomorphically substitutes Ca in apatite and, to some extent, occurs in carbonate minerals such as calcite, dolomite, and ankerite. Overall, these observations indicate that Sr is hosted primarily in barite, phosphate, and carbonate minerals within the coal discard samples.

5.2.3. Zr

The concentration of Zr is significantly high (CC $>$ 5) compared to averages levels observed in coals worldwide. SEM-EDS and TIMA data show that Zr is present in detrital zircon minerals. This observation is consistent with previous research identifying zircon as a frequent Zr-bearing mineral in coals (Karayiğit et al., 2000; Dai et al., 2006). The correlation analysis presented in Fig. 16a shows a strong positive correlation between Zr and TiO_2. This suggests a mineral association between zircon and Ti-bearing minerals rather than the incorporation of Zr within Ti-bearing minerals. Both zircon and Ti-bearing minerals are heavy and resistant, commonly concentrating in deposits due to their physical stability during alteration processes. However, Zhao et al. (2017) highlighted that Zr occurs in anatase. A moderate positive correlation between Zr and Al_2O_3 in Fig. 16b indicates the presence of Zr in Al-bearing minerals. Supporting this Karayiğit et al. (2024) reported that Zr occurs within aluminosilicate minerals. These findings align with earlier studies where Zr was not directly observed in SEM-EDS data but was inferred though correlation analysis to have an inorganic affinity within coals (Karayiğit et al., 2017, 2024).

5.2.4. Ba

The Ba concentration in the high-volatile bituminous coal discard is significantly high (CC $>$ 5) compared to values typically observed in coals worldwide. Notably, one sample from a deeper depth exhibited an exceptionally high Ba concentration of 3426.22 μg/g. SEM-EDS analysis confirms that Ba is present primarily in barite, consistent with previous studies identifying barite as a common Ba-bearing mineral in coal (Zhao et al., 2014; Karayiğit et al., 2019, 2022, 2024). Earlier research has shown a positive correlation between Ba and ash yield in Permian bituminous coals from the Guizhou Province (Dai et al., 2005). Conversely, lignite coals from the Can Basin in Turkey exhibited a moderate negative correlation between Ba and ash yield, suggesting that organic matter is the primary host of Ba in those coals (Gürdal, 2008). Additionally, Ba has been reported to isomorphically substitute K in clay minerals, with this substitution balanced by the replacement of Si^{+4} by Al^{+3}, indicating Ba's presence in silicate minerals. In medium -volatile bituminous coals from the Ordos Basin, barite, boehmite, and organic matter have been identified as the major Ba carriers (Zhao et al., 2014). In overall, these findings confirm that Ba is mainly hosted in barite, with the remaining Ba accommodated in kaolinite and other clay minerals within bituminous coal discards.

5.3. Mechanism of Ga-Sr-Zr-Ba enrichment

Enrichment refers to the mechanisms that increase the concentrations of elements in coal. Base on the above geochemistry and mineralogy of the Permian coal discards of the Witbank Coalfield, it is anticipated that the enrichment of Ga, Sr, Zr and Ba occurs. This section discusses the significant enrichment of these trace elements, by exploraring the geochemical and geological controls responsible for their

Table 4
Average concentration of trace elements (μg/g) across various depths (m) on a whole rock basis.

Depth (m)	Li	Be	Sc	Co	Ni	Cu	Zn	Ga	Rb	Sr	Y	Zr	Nb	Mo	Ba	La	Ce	Nd	Pb
1	58.93	2.36	7.98	16.9	70.71	83.43	73.14	129.08	64.71	338.24	3.66	494.71	12.47	1.8	885.57	1.66	5.56	1.42	40
2	50.96	2.07	5.94	13.06	82.29	73.79	77.36	131.66	49.5	331.19	4.12	487.43	11.12	1.7	898.24	2.85	9.07	2.8	40
3	55.96	2.04	6.88	14.72	78.14	76.14	117.36	139.08	58.57	309.49	3.84	483.14	11.61	1.79	944.08	1.83	6.09	1.94	32.75
4	60.03	2.19	6.62	17.13	74.71	81.92	77.14	155.81	57.54	387.23	4.39	489.14	12.62	2.21	1079.53	3.11	9.36	4.33	33.67
5	55.87	2.13	7.63	15.37	69.86	87.07	76.14	140.3	62.93	352.15	4.71	522.5	12.34	2.12	983.72	2.32	7.56	2.48	37

elevated concentrations.

5.3.1. Source materials

The Al_2O_3/TiO_2 ratio serves as a key indicator in determining the origin and source of sedimentary rocks (Hayashi et al., 1997) and coal seams (Zheng et al., 2017; Zhao et al., 2019a). Ratios between 3 and 8 indicate a mafic igneous rock source, values between 8 and 21 reflect intermediate igneous rocks, while ratios from 21 to 70 are typical of felsic igneous rocks (Hayashi et al., 1997). The Al_2O_3-TiO_2 plot for the Witbank Coalfield coal discard samples (Fig. 17a) shows that all samples fall within the intermediate igneous rock field. The reciprocal of the Al_2O_3/TiO_2 ratio increases as the SiO_2 content decreases in igneous rocks (Huemer, 1997). Correspondingly, the TiO_2/Al_2O_3-SiO_2 plot for these coal discard samples (Fig. 17b) indicates a predominant influence from igneous rocks. This supports earlier findings that coal seams in the Witbank Coalfields were intruded by a series of igneous rocks (Coetzee and Kisters, 2016).

The TiO_2/Al_2O_3 ratio has also been used to infer the pH of the depositional environment of coal seams. Typically, TiO_2/Al_2O_3 ratios between 0.014 and 0.048 suggest acidic conditions; values from 0.048 to 0.125 indicate neutral conditions; and ratios between 0.125 and 0.333 reflect basic conditions (Shao et al., 2022; Huemer, 1997). As shown in Fig. 17c, the TiO_2-Al_2O_3 plot reveals that the coal discards exhibit neutral pH characteristics, contrasting with the typically acidic nature of South African coals. This observation aligns with TIMA and XRD data, which demonstrated the presence of acid-neutralizing minerals such as kaolinite, calcite, dolomite, illite and muscovite. Notably, Mxinwa et al. (2020) highlighted the potential of South African coal discards to act as neutralizing agents for acid mining drainage, suggesting their use as precursor for lime neutralization.

The Zr/TiO_2 and Nb/Y ratios are key indicators for magma source discrimination (Winchester and Floyd, 1977). The Zr/TiO_2-Nb/Y plot (Fig. 17d) shows that most coal discard samples fall within the trachyandesite field, with some samples located in the trachyte field, and a few in the comendite-pantellerite, and phonolite fields. These findings suggest that the coal seams were influenced by both felsic and mafic volcanic ashes. Additionally, these results corroborate previous studies that indicated alkaline felsic ashes are rich in SiO_2, Nb, Zr and Ga, whereas mafic volcanic ashes tend to have high concentrations of Co and Ni, accompanied by depletion of Ce, La, Nd, and Y (Dai et al., 2014; Zhao et al., 2017; Zheng et al., 2017).

5.3.2. The Sr/Ba ratio and depositional environment of Witbank Coalfield coal discards

The Sr/Ba ratio is a well-established indicator for paleosalinity assessment in sedimentary deposits (Wang et al., 1979; Dai et al., 2020; Karayiğit et al., 2024) and has proven useful in coal research as well (Dai et al., 2018; Spiro et al., 2019). Typically, ratios below 1, as consistently observed in the Witbank Coalfield coal discard samples (Fig. 18), confirm a predominantly freshwater depositional environment (Wang et al., 1979; Dai et al., 2020). This finding aligns with geochemical and sedimentological studies describing peat formation in wetlands, fluvial systems, and lacustrine settings characteristics of the Witbank basin (Weeber et al., 2000; Soeder and Borglum, 2019; Netshitungulwana et al., 2022).

While Sr/Ba ratios provide valuable paleosalinity constraints, interpreting trace elements requires careful consideration of post-depositional mobility and mineralogical hosts. In the Witbank samples, trace elements such as Ga, Sr, Zr and Ba exhibit varying degrees of mobility influenced by geochemical processes like leaching, diagenesis, and groundwater interaction. For instance, Ba is frequently hosted in barite, a sulfate mineral that can form syngenetically or through diagenetic precipitation, which may concentrate Ba independently of depositional salinity (Dai et al., 2020; Karayiğit et al., 2022). SEM-EDS data confirm Sr and Ba association with barite grains (Figs. 9e and 9f), underscoring the influence of authigenic mineral formation on trace

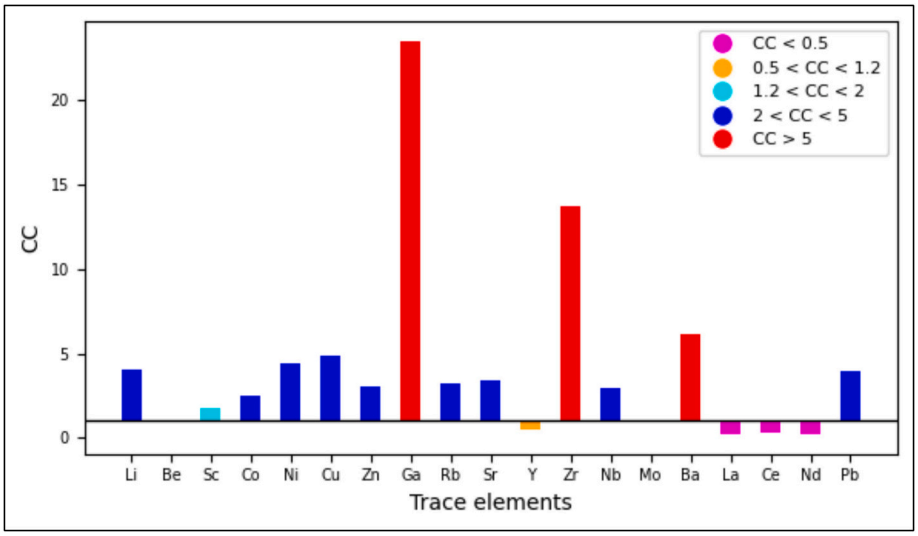

Fig. 13. Enrichment of trace elements in the coal discards of the Witbank Coalfield compared to the hard coals around the world (Ketris and Yudovich, 2009).

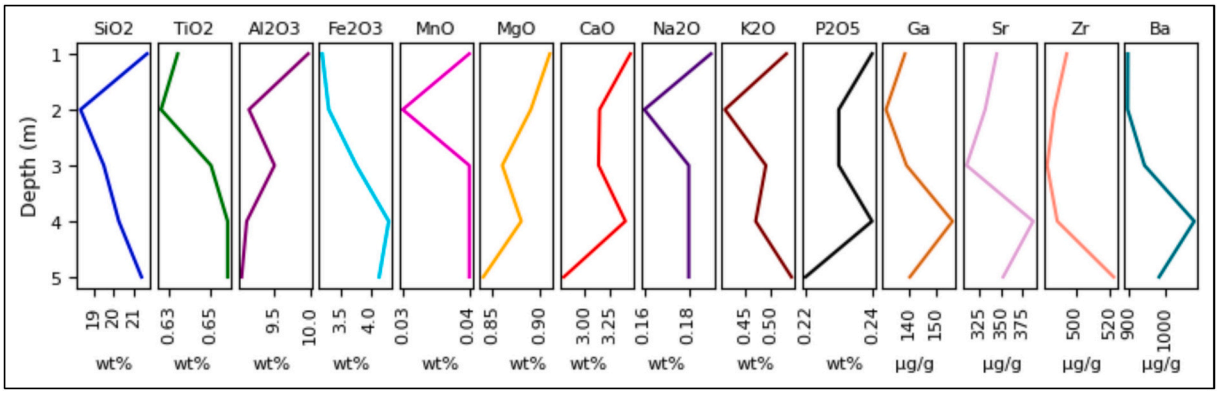

Fig. 14. Vertical distribution of major oxides in wt% and Ba, Zr, Sr, and Ga in µg/g in the coal discards.

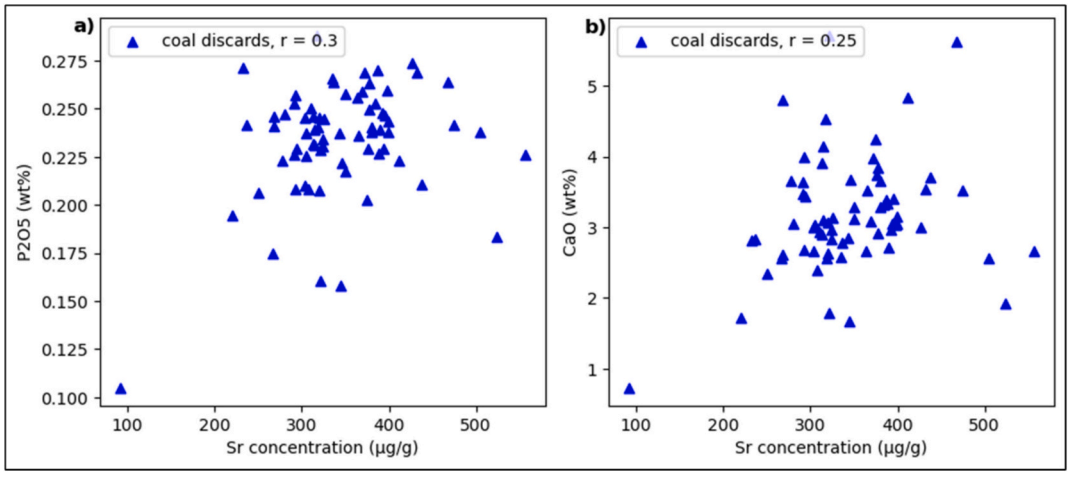

Fig. 15. Correlation analysis, a) correlation between Sr and P_2O_5, b) correlation between Sr and CaO in the coal discards.

element distribution. Siderite and pyrite presence, along with Fe-, Mn-, Mg-bearing carbonate minerals such as ankerite and dolomite, reflect redox-driven diagenetic processes and suggest an evolving geochemical environment where sulfate reduction, organic matter decay, and groundwater chemistry exert control on mineral formation and elemental partitioning (Liu et al., 2019; Wang, 2017).

Diagenesis alterations are documented by the abundance of carbonate minerals and the neutral pH signatures inferred from TiO_2/Al_2O_3 ratios (Fig. 17c), contrasting with the generally acidic nature of South African coals. The presence of acid-neutralizing minerals such as

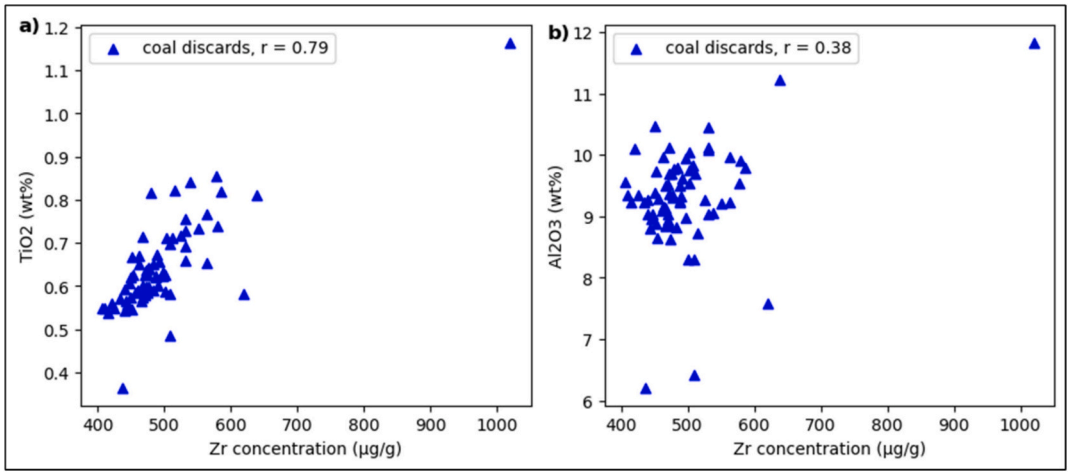

Fig. 16. Correlation analysis, a) correlation between Zr and TiO_2, b) correlation between Zr and Al_2O_3 in the coal discards.

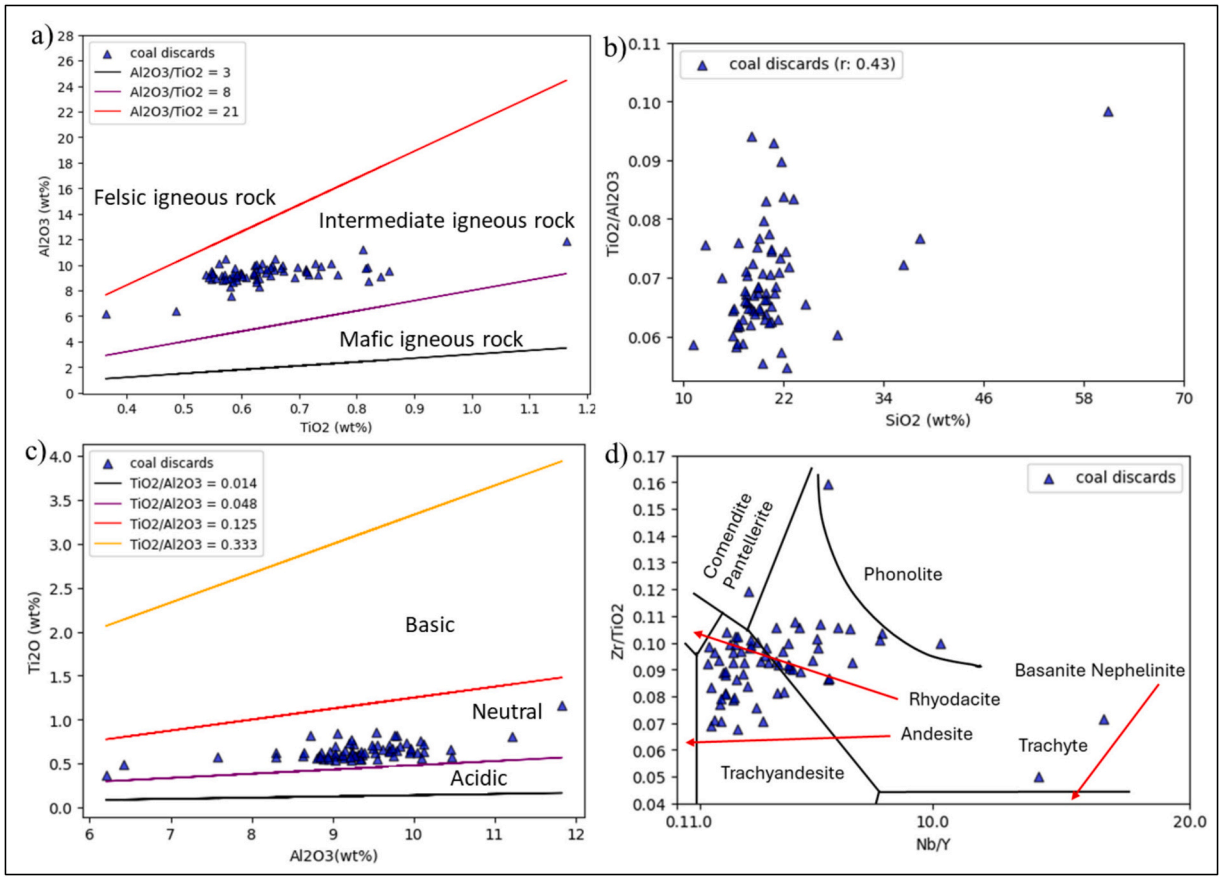

Fig. 17. Plot showing relationship between a) Al_2O_3 and TiO_2, b) TiO_2/ Al_2O_3 and SiO2, c) TiO_2 and Al_2O_3, d) Zr/ SiO_2 and Nb/Zr in the coal discards (after Winchester and Floyd, 1977).

kaolinite, calcite, dolomite, illite and muscovite supports the buffering of acidic fluids and may regulate trace element retention or remobilization (Mxinwa et al., 2020). The vertical distribution data (Fig. 14) further point to geochemical mobility related to groundwater transport. Trace elements such as Ba and Ga show enrichment at mid-depths (up to 4 m), while CaO depletion at 5 m indicates acidic groundwater dissolution of calcite (Liu et al., 2018), reflecting localized diagenetic alteration.

Ash yield, which indicates the inorganic mineral content of coal, serves as a vital sedimentological proxy, linking geochemistry and depositional environmental. In this case, ash yield shows a moderate negative correlation with the Sr/Ba (Fig. 18), supporting a freshwater depositional setting with terrigenous input, as previously suggested by Spiro et al. (2019). This correlation aligns closely with the work of Dai et al. (2018), which comprehensively analyzed the relationship between Sr/Ba ratios and ash yields in coal samples. Their study demonstrated that lower Sr/Ba ratios correspond to freshwater conditions and higher organic content, reflected by lower ash yields, whereas higher Sr/Ba ratios tend to indicate marine influence accompanied by increased mineral matter. Dai et al. (2018) highlighted that ash yield is a reliable

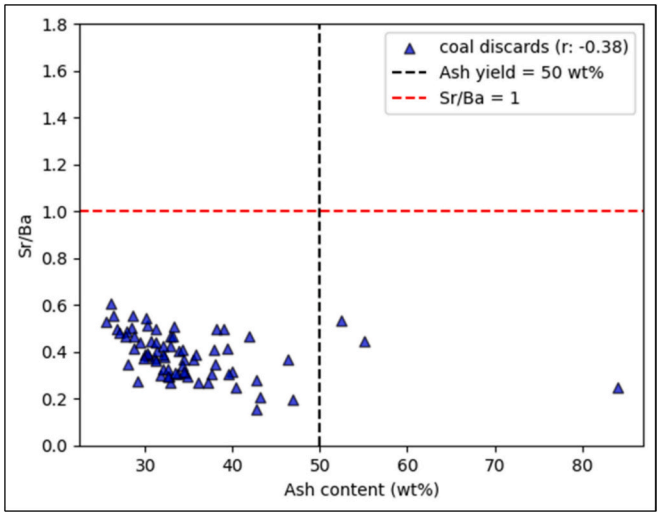

Fig. 18. Diagrams of Sr/Ba and Ash yield for coal discards.

proxy to distinguish depositional environmental when used alongside Sr/Ba and B geochemical signatures.

In the case of the present study, most samples fall below the 50 wt% ash yield threshold that defines high-ash coals (Fig. 18), indicating moderate minerals content consistent with freshwater peat accumulation with significant clastic sediment influx. The low Sr/Ba ratios and ash yields together reinforce the interpretation of coal formed predominantly under freshwater conditions. Supporting this, geochemical data show depleted levels of MgO, MnO, Na_2O, K_2O and REY, which is characteristics of minimal marine input despite the common presence of marine minerals such as pyrite, dolomite and calcite.

The geochemical composition and mineralogy of the Witbank coal discards align with regional trends observed in other South African coalfields and globally. The elevated concentrations and enrichment of Ba, Zr and Ga (CC $>$ 5) observed in this study are consistent with those reported for other bituminous coals, where Ga commonly associated with kaolinite (Wang et al., 2011; Shao et al., 2018; Zhao et al., 2019) and Zr with detrital zircon (Karayiğit et al., 2000; Dai et al., 2006). Additionally, the combined geochemical and mineralogical data support previous models of the Witbank coal seams being intruded by igneous rocks (Coetzee and Kisters, 2016), as explained by intermediate igneous rock signatures in TiO_2/Al_2O_3 ratios (Fig. 17a) and magma source discrimination plots (Fig. 17d) indicating felsic and mafic volcanic influence (Dai et al., 2014).

6. Conclusion

This study offers a comprehensive mineralogical and geochemical characterization of coal discards from the Witbank Coalfield, elucidating their formation environment as well as occurrence, distribution and enrichment of trace elements. The coal discards are dominated by quartz and kaolinite, with minor carbonate and sulfide minerals that reflect diagenetic transformations and hydrothermal influences. Trace element analyses reveal significant enrichments in gallium (Ga), strontium (Sr), zirconium (Zr) and barium (Ba). Ga is primarily associated with both kaolinite and organic matter, with an average concentration of 141.07 μg/g; Sr and Ba occur predominantly in barite, with average concentrations of 344.94 and 960.85 μg/g, respectively; and Zr is hosted in detrital zircon grains, with an average concentration of 495.39 μg/g. These elevated concentrations highlight the economic potential of these elements, indicating that targeted extraction from coal discards could be a valuable avenue for resource recovery.

The Sr/Ba rand TiO_2/Al_2O_3 ratios confirm a freshwater depositional environment with notable contributions from intermediate igneous rock sources and volcanic ash. Additionally, the negative correlation between Sr/Ba ratios and ash yields further supports terrigenous clastic input in peat formation under continental freshwater conditions. Diagenetic process and groundwater chemistry have modulated mineral abundance and trace element mobility, as evidenced by vertical variations in element concentrations and minerals assemblages. The presence of acid-neutralizing minerals such a kaolinite and carbonates suggest potential application of these coal discards in mitigating acid mine drainage, enhancing their environmental value beyond waste material. Overall, the integration of multi-technique mineralogical data and trace element geochemistry advances the understanding of depositional and post-depositional evolution of Witbank coals. It also provides a valuable framework for future studies on coal discards management, sustainable resource utilization, and the recovery of economically important elements in similar coal basins globally.

CRediT authorship contribution statement

X. Nkwamza: Writing – original draft, Visualization, Resources, Methodology, Investigation, Data curation, Conceptualization. **N. Malumbazo:** Writing – review & editing, Validation, Supervision, Funding acquisition.

Declaration of competing interest

The authors declare that they have no known competing financial interests or personal relationships that could have appeared to influence the work reported in this paper.

Acknowledgements

The authors wish to thank Seriti Coal Mine for providing access to the sampling location. Funding was provided by the Seriti Coal Mine under grant SERITI1.

Data availability

Data will be made available on request.

References

Aja, S.U., 2019. On the thermodynamic stability of illite and IS minerals. Clay Clay Miner. 67, 518–536.
ASTM D 388-99, 1999. Annual Book of ASTM Standards. Standard Classification of Coals by Rank: Gaseous Fuels; Coal and Coke. Vol. 05.06.
ASTM D 5142-09, 2009. Standard test Method for Proximate Analysis of the Analysis Sample of Coal and Coke by Instrument Procedures1: ASTM D5142/D5142–09.
ASTM D 5865-07, 2007. A standard Test Method for Gross Calorific Value of Coal and Coke: ASTM D5865/D5865-07.
Biswas, S., Wagner, N.J., Moroeng, O.M., 2024. Organic petrographic and mineralogical composition of the no. 6 coal seam of the Soutpansberg Coalfield, South Africa: Insights into paleovegetation and depositional environment. Int. J. Coal Sci. Technol. 11, 41.
Cadle, A.B., Cairncross, B., 1987. A genetic stratigraphy for the Permian coal-bearing Vryheid Formation in the east Witbank Coalfield, South Africa. S. Afr. J. Geol. 90, 219–230.
China Science and Technology Daily Report. http://www.stdaily.com/kjrb/kjrbbm/2018-04-20/content_661562.shtml/, 2018 [Accessed 15 Mar. 2025].
Cloete, H.C.C., 2012. The Estimation of Uncertainty of Measurement by X-Ray Fluorescence Spectrometry. MSc thesis. Department of Chemistry, University of Johannesburg.
Coetzee, A., Kisters, A., 2016. The 3D geometry of regional-scale dolerite saucer complexes and their feeders in the Secunda complex, Karoo Basin. J. Volcanol. Geotherm. Res. 317, 66–79.
Dai, S., Chou, C.-L., 2007. Occurrence and origin of minerals in a chamosite-bearing coal of late Permian age, Zhaotong, Yunnan, China. Am. Mineral. 92, 1253–1261.
Dai, S., Finkelman, R.B., 2018. Coal as a promising source of critical elements: progress and future prospects. Int. J. Coal Geol. 186, 155–164.
Dai, S., Ren, D., Tang, Y., Yue, M., Hao, L., 2005. Concentration and distribution of elements in late Permian coals from western Guizhou Province, China. Int. J. Coal Geol. 61, 119–137.

Dai, S., Ren, D., Chou, C.-L., Li, S., Jiang, Y., 2006. Mineralogy and geochemistry of the no. 6 coal (Pennsylvanian) in the Junger Coalfield, Ordos Basin, China. Int. J. Coal Geol. 66, 253–270.
Dai, S., Ren, D., Li, S., 2006a. Discovery of the superlarge gallium ore deposit in Jungar, Inner Mongolia, North China. Sci. Bull. 51, 2243–2252.
Dai, S., Wang, X., Zhou, Y., Hower, J.C., Li, D., Chen, W., Zhu, X., Zou, J., 2011. Chemical and mineralogical compositions of silicic, mafic, and alkali tonsteins in the late Permian coals from the Songzao Coalfield, Chongqing, Southwest China. Chem. Geol. 282, 29–44.
Dai, S., Jiang, Y., Ward, C.R., Gu, L., Seredin, V.V., Liu, H., Zhou, D., Wang, X., Sun, Y., Zou, J., Ren, D., 2012. Mineralogical and geochemical compositions of the coal in the Guanbanwusu Mine, Inner Mongolia, China: further evidence for the existence of an Al (Ga and REE) ore deposit in the Jungar Coalfield. Int. J. Coal Geol. 98, 10–40.
Dai, S., Ren, D., Chou, C.-L., Finkelman, R.B., Seredin, V.V., Zhou, Y., 2012a. Geochemistry of trace elements in Chinese coals: a review of abundances, genetic types, impacts on human health, and industrial utilization. Int. J. Coal Geol. 94, 3–21.
Dai, S., Zhang, W., Ward, C.R., Seredin, V.V., Hower, J.C., Li, X., Song, W., Wang, X., Kang, H., Zheng, L., Wang, P., 2013. Mineralogical and geochemical anomalies of late Permian coals from the Fusui Coalfield, Guangxi Province, southern China: influences of terrigenous materials and hydrothermal fluids. Int. J. Coal Geol. 105, 60–84.
Dai, S., Luo, Y., Seredin, V.V., Ward, C.R., Hower, J.C., Zhao, L., Liu, S., Zhao, C., Tian, H., Zou, J., 2014. Revisiting the late Permian coal from the Huayingshan, Sichuan, southwestern China: Enrichment and occurrence modes of minerals and trace elements. Int. J. Coal Geol. 122, 110–128.
Dai, S., Seredin, V.V., Ward, C.R., Jiang, J., Hower, J.C., Song, X., Jiang, Y., Wang, X., Gornostaeva, T., Li, X., Liu, H., Zhao, L., Zhao, C., 2014a. Composition and modes of occurrence of minerals and elements in coal combustion products derived from high-Ge coals. Int. J. Coal Geol. 121, 79–97.
Dai, S., Li, T., Jiang, Y., Ward, C.R., Hower, J.C., Sun, J., Liu, J., Song, H., Wei, J., Li, Q., Xie, P., 2015. Mineralogical and geochemical compositions of the Pennsylvanian coal in the Hailiushu Mine, Daqingshan Coalfield, Inner Mongolia, China: implications of sediment-source region and acid hydrothermal solutions. Int. J. Coal Geol. 137, 92–110.
Dai, S., Seredin, V.V., Ward, C.R., Hower, J.C., Xing, Y., Zhang, W., Song, W., Wang, P., 2015a. Enrichment of U–Se–Mo–Re–V in coals preserved within marine carbonate successions: geochemical and mineralogical data from the Late Permian Guiding Coalfield, Guizhou, China. Mineral. Deposita 50, 159–186.
Dai, S., Ji, D., Ward, C.R., French, D., Hower, J.C., Yan, X., Wei, Q., 2018. Mississippian anthracites in Guangxi Province, southern China: Petrological, mineralogical, and rare earth element evidence for high-temperature solutions. Int. J. Coal Geol. 197, 84–114.
Dai, S., Yan, X., Ward, C.R., Hower, J.C., Zhao, L., Wang, X., Zhao, L., Ren, D., Finkelman, R.B., 2018a. Valuable elements in Chinese coals: a review. Int. Geol. Rev. 60, 590–620.
Dai, S., Bechtel, A., Eble, C.F., Flores, R.M., French, D., Graham, I.T., Hood, M.M., Hower, J.C., Korasidis, V.A., Moore, T.A., Püttmann, W., 2020. Recognition of peat depositional environments in coal: a review. Int. J. Coal Geol. 219, 103383.
Dai, S., Finkelman, R.B., French, D., Hower, J.C., Graham, I.T., Zhao, F., 2021. Modes of occurrence of elements in coal: a critical evaluation. Earth Sci. Rev. 222, 103815.
Davison, R., Van Rythoven, A., 2023. Critical Mineral: Germanium. Montana Bureau of Mines and geology Fact Sheet 5. Available at:. https://doi.org/10.59691/APGQ7792 [Accessed 5 Aug. 2025].
DMRE, 2001. National Inventory of Discard and Duff Coal, South African Government, Pretoria. Available at: https://www.dmre.gov.za/Portals/0/Energy_Website/Coal/coal_discard_report.pdf [Accessed 26 January 2024].
Eriksson, P.G., Altermann, W., 1998. An overview of the geology of the Transvaal Supergroup dolomites (South Africa). Environ. Geol. 36, 179–188.
Eriksson, P.G., Schweitzer, J.K., Bosch, P.J.A., Schereiber, U.M., Van Deventer, J.L., Hatton, C.J., 1993. The Transvaal sequence: an overview. J. Afr. Earth Sci. 16, 25–51.
Falcon, L.M., Falcon, R., 1987. The petrographic composition of Southern African coals in relation to friability, hardness, and abrasive indices. J. South. Afr. Inst. Min. Metall. 87, 323–336.
Falcon, R., Ham, A., 1988. The characteristics of South African coals. J. South. Afr. Inst. Min. Metall. 88, 145–161.
Farjana, S.H., Huda, N., Mahmud, M.P., Lang, C., 2018. Towards sustainable TiO2 production: an investigation of environmental impacts of ilmenite and rutile processing routes in Australia. J. Clean. Prod. 196, 1016–1025.
Ferro, P., Banollo, F., 2019. Material selection in a critical raw material perspective. Mater. Des. 177, 107848.
Finkelman, R.B., Dai, S., French, D., 2019. The importance of minerals in coal as the hosts of chemical elements: a review. Int. J. Coal Geol. 212, 103251.
Fuller, M.P., Hamadeh, I.M., Griffiths, P.R., Lowenhaupt, D.E., 1982. Diffuse reflectance infrared spectrometry of powdered coals. Fuel 61, 529–536.
Georgakopoulos, A., 2003. Study of low rank Greek coals using FTIR spectroscopy. Energy Sources 25, 995–1005.
Gürdal, G., 2008. Geochemistry of trace elements in Çan coal (Miocene), Çanakkale, Turkey. Int. J. Coal Geol. 74, 28–40.
Hancox, P.J., Götz, A.E., 2014. South Africa's coalfields—A 2014 perspective. Int. J. Coal geol. 132, 170–254.
Hao, H., Zhang, M., Wang, J., Fu, Z., Balaji, P., Jiang, S., 2022. Barium in coal and coal combustion products: distribution, enrichment, and migration. Energy Explor. Exploit. 40, 889–907.
Hayashi, K.I., Fujisawa, H., Holland, H.D., Ohmoto, H., 1997. Geochemistry of~ 1.9 Ga sedimentary rocks from northeastern Labrador, Canada. Geochim. Cosmochim. Acta 61, 4115–4137.
Hower, J.C., Berti, D., Hochella Jr., M.F., Mardon, S.M., 2018. Rare earth minerals in a "no tonstein" section of the Dean (Fire Clay) coal, Knox County, Kentucky. Int. J. Coal Geol. 193, 73–86.
Huemer, H., 1997. Multistage evolution of a volcanic suite in the Eastern Mecsek Mountains, Southern Hungary. Mineral. Petrol. 59, 101–120.
Jiu, B., Huang, W., Sun, Q., 2021. Distribution characteristics and enrichment model of germanium in coal: an example from the Yimin Coalfield, Hailar Basin, China. Nat. Resour. Res. 30, 725–740.
Jiu, B., Huang, W., Spiro, B., Hao, R., Mu, N., Wen, L., Hao, H., 2023. Distribution of Li, Ga, Nb, and REEs in coal as determined by LA-ICP-MS imaging: a case study from Jungar coalfield, Ordos Basin, China. Int. J. Coal Geol. 267, 104184.
Jones and Wagener, 2017. Rietspruit Mine - Mine Closure Operations: Old Tailings Dam – Geotechnical Investigation and Probability of Failure Assessment. Report No.: JW185/16/F070 - Rev 2.
Karayiğit, A.I., Gayer, R.A., Querol, X., Onacak, T.Ü.R.K.A.Y., 2000. Contents of major and trace elements in feed coals from Turkish coal-fired power plants. Int. J. Coal Geol. 44, 169–184.
Karayiğit, A.I., Bircan, C., Mastalerz, M., Oskay, R.G., Querol, X., Lieberman, N.R., Türkmen, I., 2017. Coal characteristics, elemental composition and modes of occurrence of some elements in the İsaalan coal (Balıkesir, NW Turkey). Int. J. Coal Geol. 172, 43–59.
Karayiğit, A.I., Oskay, R.G., Gayer, R.A., 2019. Mineralogy and geochemistry of feed coals and combustion residues of the Kangal power plant (Sivas, Turkey). Turk. J. Earth Sci. 28, 438–456.
Karayiğit, A.I., Azeri, N., Oskay, R.G., Hower, J.C., 2022. Zeolite and associated mineral occurrences in high-Sulphur coals from the middle Miocene upper coal seam from underground mines in the Çayirhan coalfield, (Beypazarı, Central Turkey). Int. J. Coal Geol. 256, 104010.
Karayiğit, A.İ., Oskay, R.G., Bircan, C., 2024. Mineralogical, Petrographical and Geochemical Properties of the late Oligocene Coal Seam (Seam-VI): Insights into Elemental Enrichments and Palaeodepositional Environment (İbrice field, Thrace Basin). Yerbilimleri 45, 1–51.
Ketris, M.Á., Yudovich, Y.E., 2009. Estimations of Clarkes for Carbonaceous biolithes: World averages for trace element contents in black shales and coals. Int. J. Coal Geol. 78, 135–148.
Kolker, A., Scott, C., Lefticariu, L., Mastalerz, M., Drobniak, A., Scott, A., 2021. Trace element partitioning during coal preparation: Insights from US Illinois Basin coals. Int. J. Coal Geol. 243, 103781.
Li, J., Zhuang, X., Yuan, W., Liu, B., Querol, X., Font, O., Moreno, N., Li, J., Gang, T., Liang, G., 2016. Mineral composition and geochemical characteristics of the Li-Ga-rich coals in the Buertaohai-Tianjiashipan mining district, Jungar Coalfield, Inner Mongolia. Int. J. Coal Geol. 167, 157–175.
Lin, R., Soong, Y., Granite, E.J., 2018. Evaluation of trace elements in US coals using the USGS COALQUAL database version 3.0. Part I: rare earth elements and yttrium (REY). Int. J. Coal Geol. 192, 1–13.
Lin, R., Soong, Y., Granite, E.J., 2018a. Evaluation of trace elements in US coals using the USGS COALQUAL database version 3.0. Part II: Non-REY critical elements. Int. J. Coal Geol. 192, 39–50.
Lin, R., Stuckman, M., Howard, B.H., Banka, T.L., Roth, E.A., Macala, M.K., Lopano, C., Soong, Y., Granite, E.J., 2018b. Application of sequential and hydrothermal treatment for characterization and enrichment of rare earth elements from coal fly ash. Fuel 232, 124–133.
Liu, J., Ward, C.R., Graham, I.T., French, D., Dai, S., Song, X., 2018. Modes of occurrence of non-mineral inorganic elements in lignites from the Mile Basin, Yunnan Province, China. Fuel 222, 146–155.
Liu, J., Spiro, B.F., Dai, S., French, D., Graham, I.T., Wang, X., Zhao, L., Zhao, J., Zeng, R., 2021. Strontium isotopes in high-and low-Ge coals from the Shengli Coalfield, Inner Mongolia, northern China: new indicators for Ge source. Int. J. Coal Geol. 233, 103642.
Liu, J., Feng, J., Gao, Z., Wang, M., Li, G., Shi, M., Zhang, H., 2019. Hydrochemical characteristics and quality assessment of groundwater for drinking and irrigation purposes in the Futuan River Basin, China. Arab. J. Geosci. 12, 560.
Liu, L., Liu, Q., Algeo, T., Zhang, H., Yang, Y., Peng, G., Zhang, S., Hong, H., Liu, D., 2021a. Mineralogy, geochemistry, and genesis of kaolinitic claystone deposits in the Datong Coalfield, northern China. Clay Clay Miner. 69, 68–93.
Maphoso, R., Malumbazo, N., Vatsha, B., Nwaila, G., 2024. Critical raw material: Characterisation and froth floatation as a preconcentration technique of weathered and non-weathered coal discards from Mpumalanga. In: Southern Africa rare Earths, 2nd International Conference 2024, South African Institute of Mining and Metallurgy, Swakopmund, Namibia, 19-20 June.
Martin, K.A., Chao, S.S., 1988. Structural group analysis of argonne premium coals by FTIR spectroscopy. Prepr. Pap., Am. Chem. Soc., Div. Fuel Chem. 33, 220–230 (United States), 33(CONF-8809161-).
Mastalerz, M., Bustin, R.M., 1993. Electron microprobe and micro-FTIR analyses applied to maceral chemistry. Int. J. Coal Geol. 24, 333–345.
Mastalerz, M., Bustin, R.M., 1996. Application of reflectance micro-Fourier Transform infrared analysis to the study of coal macerals: an example from the late Jurassic to early cretaceous coals of the Mist Mountain Formation, British Columbia, Canada. Int. J. Coal Geol. 32, 55–67.
Mastalerz, M., Drobniak, A., Eble, C., Ames, P., McLaughlin, P., 2020. Rare earth elements and yttrium in Pennsylvanian coals and shales in the eastern part of the Illinois Basin. Int. J. Coal Geol. 231, 103620.

Maya, M., Musekiwa, C., Mthembi, P., Crowley, M., 2015. Remote sensing and geochemistry techniques for the assessment of coal mining pollution, Emalahleni (Witbank), Mpumalanga. S. Afr. J. Geom. 4, 174–188.
Misz-Kennan, M., Fabiańska, M.J., 2011. Application of organic petrology and geochemistry to coal waste studies. Int. J. Coal Geol. 88, 1–23.
Modiba, D.G., Wagner, N.J., 2024. An assessment of rare Earth elements in borehole cores from the Ermelo, Witbank and Waterberg Coalfields, South Africa: Focus on mode of occurrence. J. South. Afr. Inst. Min. Metall. 124, 559–566.
Mxinwa, S., Deenanath, E.D., Robertson, S.W., Ndlovu, S., Basson, P., 2020. The application of coal discards for acid mine drainage neutralization. J. South Afr. Inst. Min. Metall. 120, 531–540.
Netshitungulwana, K.R.T., Gauert, C., Vermeulen, D., Yibas, B., Shai, M., Lusunzi, R., 2022, November. Geochemical characterisation of the Witbank coalfield geological strata and assessment of potential metal impact on the receiving environment. In: Proceedings of the International Mine Water Association 2022 Conference Reconnect, Christchurch, New Zealand (6–10).
Oikonomopoulos, I.K., Perraki, M., Tougiannidis, N., Perraki, T., Frey, M.J., Antoniadis, P., Ricken, W., 2013. A comparative study on structural differences of xylite and matrix lignite lithotypes by means of FT-IR, XRD, SEM and TGA analyses: an example from the Neogene Greek lignite deposits. Int. J. Coal Geol. 115, 1–12.
Orem, W.H., Finkelman, R.B., 2005. US geological Survey, Reston, VA, USA. Sediments, diagenesis, and sedimentary rocks. Treat. Geochem. 7, 191.
Öztaş, N.A., Yürüm, Y., 2000. Pyrolysis of Turkish Zonguldak bituminous coal. Part 1. Effect of mineral matter. Fuel 79, 1221–1227.
Painter, P.C., Snyder, R.W., Starsinic, M., Coleman, M.M., Kuehn, D.W., Davis, A., 1981. Concerning the application of FT-IR to the study of coal: a critical assessment of band assignments and the application of spectral analysis programs. Appl. Spectrosc. 35, 475–485.
Parham, W.E., 1969. Halloysite-rich tropical weathering products of Hong Kong. In Proc. Int. Clay Conf. Tokyo. 1, 393–402.
Pinetown, K.L., 2007. Quantitative Evaluation of Minerals in Coal Deposits in the Witbank and Highveld Coalfields and the Potential Impact on Acid Mine Drainage (Masters' thesis). University of the Free State.
Querol, X., Klika, Z., Weiss, Z., Finkelman, R.B., Alastuey, A., Juan, R., López-Soler, A., Plana, F., Kolker, A., Chenery, S.R.N., 2001. Determination of element affinities by density fractionation of bulk coal samples. Fuel 80, 83–96.
Rerani, V.P., Mabowa, H.M., Wagner, N.J., 2024. Characterization of rare earth element-bearing mineral phases present in south African coal ash using mineral liberation analysis. Fuel 368, 131661.
Seredin, V.V., 2012. From coal science to metal production and environmental protection: a new story of success commentary. Int. J. Coal Geol. 90, 1–3.
Seredin, V.V., Finkelman, R.B., 2008. Metalliferous coals: a review of the main genetic and geochemical types. Int. J. Coal Geol. 76, 253–289.
Seredin, V.V., Dai, S.F., Sun, Y.Z., Chekryzhov, I.Y., 2013. Coal deposits as promising sources of rare metals for alternative power and energy-efficient technologies. Appl. Geochem. 31, 1–11.
Shao, P., Wang, W., Chen, L., Duan, P., Qian, F., Ma, M., Xiong, W., Yu, S., 2018. Distribution, occurrence, and enrichment of gallium in the Middle Jurassic coals of the Muli Coalfield, Qinghai, China. J. Geochem. Explor. 185, 116–129.
Shao, P., Hou, H., Wang, W., Qin, K., Wang, W., 2022. Distribution and enrichment of Al-Li-Ga-REEs in the High-Alumina coal of the Datong Coalfield, Shanxi Province, China. Ore Geol. Rev. 140, 104597.
Soeder, D.J., Borglum, S.J., 2019. The Fossil Fuel Revolution: Shale Gas and Tight Oil. Elsevier.
Spiro, B.F., Liu, J., Dai, S., Zeng, R., Large, D., French, D., 2019. Marine derived 87Sr/86Sr in coal, a new key to geochronology and palaeoenvironment: Elucidation of the India-Eurasia and China-Indochina collisions in Yunnan, China. Int. J. Coal Geol. 215, 103304.
Sun, B., Liu, Y., Tajcmanova, L., Liu, C., Wu, J., 2022. In-situ analysis of the lithium occurrence in the no. 11 coal from the Antaibao mining district, Ningwu Coalfield, northern China. Ore Geol. Rev. 144, 104825.
Swaine, D.J., 1990. Trace Elements in Coal. Butterworths, London, p. 278.
Vassilev, S.V., Vassileva, C.G., 1996. Occurrence, abundance and origin of minerals in coals and coal ashes. FPT 48, 85–106.
Vo, T.L., Nash, W., Del Galdo, M., Rezania, M., Crane, R., Nezhad, M.M., Ferrara, L., 2022. Coal mining wastes valorization as raw geomaterials in construction: a review with new perspectives. J. Clean. Prod. 336, 130213.
Wagner, M., Bielowicz, B., Misiak, J., 2019. Analysis of the occurrence of critical elements and raw materials in Polish lignite deposits with particular emphasis on coal ashes. In IOP Confer. Ser.: Earth Environ. Sci. 214, 012026.
Wang, Y.Y., Guo, W.Y., Zhang, G.D., 1979. Application of some geochemical indicators in determining the sedimentary environment of the Funing Group (Paleogene), Jinhu Depression, Kiangsu Province. J. Tongji Univ. 2, 51–60 (in Chinese with English abstract).
Wang, P.P., 2017. Enrichment and Differentiation Mechanism of Minerals and Trace Elements in the Late Permian Coals from Eastern Yunnan and Western Guizhou Province. PhD thesis. China University of Mining and Technology (Beijing). Beijing (in Chinese with English abstract).
Wang, Q., Yan, Q., Zhang, Y., Zhou, F., 2022. Enrichment Mechanism of Lithium in late Permian Coals in the Bijie Area, Guizhou, China. ACS Omega 7, 16361–16370.
Wang, W., Qin, Y., Liu, X., Zhao, J., Wang, J., Wu, G., Liu, J., 2011. Distribution, occurrence and enrichment causes of gallium in coals from the Jungar Coalfield, Inner Mongolia. Sci. China Earth Sci. 54, 1053–1068.
Wang, X., Dai, S., Chou, C.-L., Zhang, M., Wang, J., Song, X., Wang, W., Jiang, Y., Zhou, Y., Ren, D., 2012. Mineralogy and geochemistry of late Permian coals from the Taoshuping Mine, Yunnan Province, China: Evidences for the sources of minerals. Int. J. Coal Geol. 96, 49–59.
Wang, X., Feng, Q., Meng, Q., Liu, F., Cao, Q., Liu, G., 2021. Distribution and modes of occurrence of uranium in coals of Eastern Yunnan, China. Int. J. Coal Sci. Technol. 8, 1262–1271.
Weeber, S.L., Cairncross, B., Falcon, R., 2000. Mineralogical, petrographic and geological controls on coal ash fusion temperature from New Clydesdale Colliery, Witbank Coalfield, South Africa. J. South. Afr. Inst. Min. Metall. 100, 181–190.
Winchester, J.A., Floyd, P.A., 1977. Geochemical discrimination of different magma series and their differentiation products using immobile elements. Chem. Geol. 20, 325–343.
Xue, H., Dong, X., Fan, Y., Ma, X., Yao, S., 2023. Study of structural transformation and chemical reactivity of kaolinite-based high ash slime during calcination. Minerals 13, 466.
Yuan, Y., Tang, S., Zhang, S., 2019. Concentrations and modes of occurrence of some potentially valuable and toxic elements in the no. 5 coal from the Yanzishan Mine, Datong Coalfield, Shanxi Province, China. Energy Explor. Exploit. 37, 1694–1720.
Zhao, C., Liu, B., Ma, J., Liu, S., Blokhin, M.G., 2017. Occurrence of rubidium and cesium in Iqe coal, Qinghai-Tibet Plateau: evidence from sequential chemical extraction experiment. Energy Explor. Exploit. 35, 376–387.
Zhao, C.L., Sun, Y.Z., Xiao, L., Qin, S.J., Wang, J.X., Duan, D.J., 2014. The occurrence of barium in a Jurassic coal in the Huangling 2 Mine, Ordos Basin, northern China. Fuel 128, 428–432.
Zhao, L., Dai, S., Nechaev, V.P., Nechaeva, E.V., Graham, I.T., French, D., 2019. Enrichment origin of critical elements (Li and rare earth elements) and a Mo-U-Se-Re assemblage in Pennsylvanian anthracite from the Jincheng Coalfield, southeastern Qinshui Basin, northern China. Ore Geol. Rev. 115, 103184.
Zhao, L., Dai, S., Nechaev, V.P., Nechaeva, E.V., Graham, I.T., French, D., Sun, J., 2019a. Enrichment of critical elements (Nb-Ta-Zr-Hf-REE) within coal and host rocks from the Datanhao mine, Daqingshan Coalfield, northern China. Ore Geol. Rev. 111, 102951.
Zheng, Q., Liu, Q., Shi, S., 2016. Mineralogy and Geochemistry of Ammonian Illite in Intra-Seam Partings in Permo-Carboniferous Coal of the Qinshui Coalfield.
Zheng, X., Wang, Z., Wang, L., Xu, Y., Liu, J., 2017. Mineralogical and geochemical compositions of the lopingian coals and carbonaceous rocks in the Shugentian coalfield, Yunnan, China: with emphasis on Fe-bearing minerals in a continental-marine transitional environment. Minerals 7, 170.